Cross-dimensional Relaxation in Fermi-Fermi Mixtures

Carolin Hahn

München 2009

Cross-dimensional Relaxation in Fermi-Fermi Mixtures

Carolin Hahn

Diplomarbeit
an der Fakultät für Physik
der Ludwig–Maximilians–Universität
München

München, Juni 2009

Erstgutachter: Prof. Dr. Theodor Hänsch
Zweitgutachter: Prof Dr. Stefan Kehrein

Contents

Chapter 1

Introduction

When the theoretical foundations of what we know today as Bose-Einstein and Fermi-Dirac statistics were laid, the experimental realization of some of their most intriguing predictions was far out of reach.

The notion of Bose statistics dates back to a paper written by Satyendranath Bose in 1924, in which he used a statistical argument to derive the black-body photon spectrum. Rejected by several journals, he sent it to Albert Einstein, who translated it into German and had it published [1]. Einstein then extended the idea of Bose's counting statistics to the case of noninteracting atoms [2, 3]. A peculiar feature of this distribution over quantized energy levels of identical particles with integer spin (*bosons*) is that at very low but finite temperatures a large fraction of the atoms occupy the lowest energy state, a phenomenon now known as Bose-Einstein condensation.

The distribution function for identical particles with half-integer spin (*fermions*) was discovered shortly after by Enrico Fermi and Paul Dirac working independently of each other [4, 5]. Due to the Pauli exclusion principle, which forbids any two identical fermions from occupying the same quantum state, fermions cannot condense. Instead, at very low temperatures fermions successively fill up the lowest energy states, forming the so-called "Fermi sea".

1.1 Ultracold atoms

After its theoretical prediction, it took more than 70 years – and the development of more and more refined techniques – until the first Bose-Einstein condensate was experimentally realized in dilute gases of rubidium and sodium atoms in 1995 [6, 7]. The transition to BEC occurs when the thermal de Broglie wavelength λ_{dB} of the particles becomes comparable to the inter-particle distance and the wave functions of the particles start to overlap. This is termed the "quantum-degenerate regime". The phase transition to BEC is of a purely quantum-statistical nature, and is not induced by interactions between the particles, which play an important role in most real systems. As the thermal de Broglie wavelength is inversely proportional to the square root of the temperature, BEC can in principle be

achieved by simply cooling a gas to sufficiently low temperatures. In most gases, however, cooling leads to the formation of clusters and molecules, and therefore a phase transition to a liquid or solid state will occur before the quantum-degenerate regime is reached. This problem is circumvented by working at ultralow densities (typically $\sim 10^{14}$ cm^{-3}), where the timescale for liquefaction or solidification by inelastic three-body collisions in the gas is much longer than that of thermal equilibration processes by means of elastic two-body collisions.

The strong current interest in cold atoms is due largely to two outstanding properties: They are dilute, i.e. weakly interacting since the average inter-particle distance is much larger than the scattering length; and, moreover, they can be cooled into the quantum degenerate regime, where the individual atomic wave packets start to overlap and macroscopic quantum mechanical behavior emerges.

A few years after degenerate Bose gases were realized, the cooling and trapping schemes developed there were adapted and applied to fermions. This proved challenging, since evaporative cooling of a single-species fermionic gas is not possible due to the Pauli principle. This difficulty is overcome by performing *sympathetic cooling* with mixtures of two types of atoms, either two different fermions (which could either be different hyperfine states of the same fermionic isotope, or different fermionic isotopes) or a boson and a fermion.

In early experiments, ^{40}K [8] and ^{6}Li atoms [9, 10] were cooled to about one-quarter of the Fermi temperature, where emergent Fermi pressure was observed, as well as Pauli blocking of collisions and deviations of the total energy and momentum distributions from those of a classical gas. More recently, fermionic alkali atoms have been cooled to temperatures well below one-tenth of their Fermi temperature.

A new direction in the investigation of dilute quantum gases has been initiated by the production and subsequent Bose-Einstein condensation of diatomic molecules from a gas of fermionic atoms [11, 12, 13]. Feshbach resonances are essential to these experiments, since they make it possible to tune the atom-atom scattering length over a wide range and even change its sign [14, 15, 16]. It has thus become possible to study Cooper pairing and Bardeen-Cooper-Schrieffer (BCS) superfluidity close to the BEC-BCS crossover as theoretically proposed by Leggett in 1980, who pointed out that fermionic superfluidity (or superconductivity) and a molecular BEC can be regarded as two limiting cases of a more general theory, with a smooth crossover conntecting the two [17]. The expected critical temperature at the crossover and on the molecular side is sufficiently high to lie within experimental reach, in contrast to weakly interacting Fermi gases, where the predicted critical temperature for the superfluid state is extremely low [18]. Since their experimental realization, important physical characteristics of resonant Fermi superfluids have been probed, such as the pairing gap [19] and the appearance of vortices in rotating superfluids [20].

Further exciting possibilities opened up with the creation of the first quantum degenerate mixture consisting of two different fermionic species, ^{6}Li and ^{40}K [21, 22] and the formation of heteronuclear Fermi-Fermi molecules [23].

So far, no heteronuclear molecular BEC has been realized, but the permanent dipole moment of the ^{6}Li–^{40}K molecules and the resulting long-range dipole-dipole interaction

makes this extremely interesting, as the creation of a polar BEC would open up the possibility of studying, for example, supersolid phases, which have been recently predicted theoretically [24].

Another theoretical prediction that could possibly be explored in the Fermi-Fermi mixture of ^{6}Li and ^{40}K is the phase transition to the so-called Fulde-Ferrell-Larkin-Ovchinnikov (FFLO) state [25, 26]. In the strongly interacting regime accessed by means of Feshbach resonances, theory predicts that in the case of mismatched Fermi surfaces a two-component superfluid Fermi gas in an optical lattice can undergo a phase transition towards an inhomogeneous superfluid state with Cooper pairs of nonzero momentum [27]: the FFLO state.

Therefore, ultracold Fermi gases are highly tunable quantum many-body systems and may in the future give new insight into such open fundamental questions of condensed matter physics as the origin of high-temperature superconductivity.

Until now, apart from lithium and potassium a number of other fermonic species have been trapped and cooled: metastable ^{3}He*, ^{53}Cr, ^{87}Sr, ^{171}Yb, ^{173}Yb, ^{199}Hg, ^{201}Hg [28, 29, 30, 31, 32, 33, 34][1], but only one mixture of two different fermionic species has been realized, ^{6}Li and ^{40}K in our lab, in Innsbruck and in Amsterdam [36].

1.2 Cross-dimensional rethermalization

In ultracold, dilute gases the interactions between particles are characterized by the s-wave scattering length a. Due to the low temperatures achieved and the lack of long-range or anisotropic interactions, the value of a determines a wide variety of equilibrium and dynamical properties of quantum degenerate gases. In many ultracold gas experiments, as mentioned above, a can be tuned from $-\infty$ to ∞ by means of Feshbach resonances [14, 15, 37], enabling the experimenter to select any desired interaction strength. Further, the efficiency of cooling processes relies on large elastic collision rates, which are proportional to a^2. In quantum gas experiments it is therefore crucial that one can accurately determine the scattering properties of dilute ultracold gases.

Monroe and co-workers demonstrated in their pioneering work with ultracold ^{133}Cs atoms [38] that the elastic collision cross section σ, which is equal to $8\pi a^2$ for identical noncondensed bosons, can be determined by means of a relatively simple rethermalization measurement starting with a nonequlibrium gas. In this measurement, the rethermalization rate for a gas in the so-called "collisionless regime" – defined by a collision rate much lower than the trap periods of the atoms, cf. chapter 2 – was measured by selectively removing energy from the gas in one spatial dimension and observing its subsequent cross-dimensional rethermalization (CDR). In such an experiment, the relaxation is driven by elastic collisions, and a detailed analysis based on Enskog's equation showed that the relaxation rate is proportional to the mean rate of collisions with a proportionality constant α that denotes the average number of collisions per particle required for thermalization

[1] For the isotopes ^{111}Cd, ^{113}Cd this has not been shown beyond doubt, see Ref. [35].

[39]. Various analytical and numerical studies have found that α is between 2.5 and 2.7 [38, 39, 40, 41, 42, 43].

Goldwin *et al.* extended the method of cross-dimensional rethermalization to probe the s-wave scattering length between bosonic and fermionic atoms in Bose-Fermi mixtures [44, 45]. In this case collisions between identical fermions are suppressed due to the Pauli principle, so that the collision rate per fermion in the mixture depends only on the number of bosons. It was shown that, in analogy with the single-species case, the relaxation rate of the fermions is proportional to the mean rate of collisions per fermion, with a proportionality constant β that reflects the mean number of collisions per fermion needed for rethermalization. The mass difference between the bosons and fermions can lead to a factor of 5 difference in β between light and heavy fermions in mixtures of experimental interest.

1.3 This thesis

In this thesis, a generalized kinetic model of cross-dimensional relaxation is developed that allows CDR in Fermi-Fermi mixtures to be described in terms of the masses and particle numbers of the fermions involved. Predictions are made for relaxation rates in different Fermi-Fermi mixtures. These predictions are tested and confirmed by means of detailed classical Monte Carlo simulations of the relaxation process.

Based on the predictions of this model, we intended to perform the first CDR measurement probing the interspecies collisional cross-section of an ultracold, dilute, non-degenerate mixture of two fermionic species, lithium and potassium. Of special interest to us was the s-wave scattering length between atoms prepared in the ^{6}Li $|F = 1/2, m_F = 1/2\rangle$ and ^{40}K $|9/2, -9/2\rangle$ states, whose tuning by means of a Feshbach resonance has recently led to the first production of ultracold diatomic molecules composed of two different fermionic atomic species [23]. Our plan was to first measure the collision cross-section at an external magnetic guidance field of 20 G far away from the Feshbach resonance at around 155 G. A magnetic field of this strength has a negligible tuning effect on the scattering length, so that one in principle obtains information on the absolute value of the interspecies scattering length at 0 G. As a next step, we were planning to use the same experimental routine to map out the Feshbach resonance, where the elastic scattering cross section changes dramatically. In order to do so, CDR measurements would be performed at varying magnetic fields in the vicinity of the resonance and one would expect significant changes in the relaxation speed. This thesis is organized as follows. Chapter 2 provides the theoretical background essential for the theoretical work and the experiments presented later on. My theoretical work on cross-dimensional rethermalization in Fermi-Fermi mixtures is accounted for in chapter 3. This chapter constitutes the main part of the work done during this thesis. The generalized kinetic model is discussed extensively, and predictions for the relaxation rates in arbitrary mixtures are derived. An in-depth treatment is given of the Monte Carlo simulations programmed to test these predictions. Finally, values for the number of collisions per fermion are tabulated for a variety of possible mixtures. For reasons of clarity some

calculations that were crucial in the derivation of the kinetic model have been put in a dedicated section in appendix A. An outline of the experiment is given in chapter 4; there our procedure is described in detail, measurement parameters are discussed and failure modes are analyzed.

Chapter 2

Theory

This chapter presents the theoretical concepts that are essential for both the simulations and the experiments described in this thesis.

Section 2.1 gives an outline of the thermometry of ultracold gases and provides equations needed for the analysis of the experimental conditions described in chapter 4. In section 2.2 basic scattering theory is reviewed and threshold energies are given for p-wave scattering of the species used in the experiment. Finally, section 2.3 discusses the basics of the optical dipole trap, the type of trap used in the experiment.

2.1 Ultracold gases

The theoretical treatment of cross-dimensional relaxation and the Monte Carlo simulations presented in this thesis assume a classical gas at low temperatures. While classical behavior of the gas is guaranteed for all temperatures in the simulations, quantum statistics has to be considered when experimenting with "real" atoms, since at sufficiently low temperatures the gas no longer behaves classically but rather requires a quantum statistical treatment. It is therefore important to understand the onset of quantum degeneracy so one can ensure that the experiments are performed at temperatures where a classical treatment of the atoms is appropriate.

This section introduces basic concepts of the quantum statistics of trapped atomic gases and derives intra-trap and time of flight density distributions for fermionic and classical gases. As they are not of interest in this thesis, bosons are not treated in detail. The reader interested in more information on the subject in general is referred to textbooks on quantum mechanics and quantum statistics, e.g. [46, 47, 48, 49]. A more detailed treatment of the physics of Fermi gases can be found in a number of review articles, e.g. [50, 51, 52].

2.1.1 Quantum statistics of fermions

According to quantum mechanics, the total wave function of a gas of identical particles has to be either symmetric or anti-symmetric under exchange of any two particles in

order to describe a physical state. Particles which have a many-particle wave function that is symmetric under particle exchange are called bosons, while particles with an anti-symmetric many-particle wave function are referred to as fermions. Whether a given particle is a boson or a fermion is connected to the spin of the particles by the spin-statistics theorem [53], which identifies particles with integer spin as bosons and those with half-integer spin as fermions. For the remainder of this section, the focus will be on fermions only.

Using the grand canonical partition function, one can derive the Fermi-Dirac distribution function $n_{FD}(\varepsilon_i)$, which describes the mean number of fermions in a single particle energy eigenstate with energy ε_i. It is given by [49]

$$n_{FD}(\varepsilon_i) = \frac{1}{e^{\beta(\varepsilon_i - \mu)} + 1} \,, \tag{2.1}$$

where $\beta = (k_B T)^{-1}$ is a measure for the temperature, k_B is Boltzmann's constant and μ is the chemical potential which describes the decrease in energy associated with removing one particle from the ensemble. The chemical potential is implicitly fixed by the normalization condition

$$\sum_{\varepsilon_i} n_{FD}(\varepsilon_i) = N \,, \tag{2.2}$$

where the sum runs over all energy eigenstates of the system and yields the total atom number N. Due to the anti-symmetry of their wave function, no two fermions can occupy the same quantum state simultaneously, so the mean occupation number $n_{FD}(\varepsilon_i)$ can only assume the values between zero and one. The chemical potential may assume any real value.

Density of states

A classical particle with mass m trapped in a harmonic potential $V_{ho}(\vec{r})$ can be described by the single-particle Hamiltonian

$$H = \frac{1}{2m}\left(p_x^2 + p_y^2 + p_z^2\right) + V_{ho}(\vec{r}) \quad \text{with} \quad V_{ho}(\vec{r}) = \frac{m}{2}\left(\omega_x^2 x^2 + \omega_y^2 y^2 + \omega_z^2 z^2\right) \,, \tag{2.3}$$

where ω_i are the angular trapping frequencies. Since the energy spectrum of a three-dimensional harmonic oscillator is known exactly, the chemical potential can be calculated directly for any given total particle number and temperature. With knowledge of the chemical potential one can derive occupation numbers and density and momentum distributions for a harmonically trapped ideal quantum gas.

In typical experiments, however, a large number of atoms are trapped and the thermal energy is much larger than the level spacing, $k_B T \gg \hbar\omega$. It is therefore permissible – and convenient for calculational purposes – to approximate the discrete spectrum of energy levels ε_i, by a continuous density of states $g(\varepsilon)$. This can be derived in the following way. The energy levels of the harmonic oscillator are

$$\varepsilon\left(n_x, n_y, n_z\right) = \left(n_x + \frac{1}{2}\right)\hbar\omega_x + \left(n_y + \frac{1}{2}\right)\hbar\omega_y + \left(n_z + \frac{1}{2}\right)\hbar\omega_z \,, \tag{2.4}$$

where the numbers n_i assume integer values $0, 1, 2, \ldots$ For energies large compared with $\hbar\omega_i$, one may treat the n_i as continuous variables and neglegt the zero-point motion. In order to determine the number of states $G_{ho}(\varepsilon)$ with energy less than a given value ε, one can introduce a coordinate system defined by the three variables $\varepsilon_i = \hbar\omega_i n_i$, in terms of which the plane $\varepsilon = \sum \varepsilon_i$ is a surface of constant energy. $G(\varepsilon)$ is therefore proportional to the volume in the first octant bounded by the plane [54],

$$G_{ho}(\varepsilon) = \frac{1}{\hbar\bar{\omega}^3} \int_0^{\varepsilon} d\varepsilon_x \int_0^{\varepsilon-\varepsilon_x} d\varepsilon_y \int_0^{\varepsilon-\varepsilon_x-\varepsilon_y} d\varepsilon_z = \frac{\varepsilon^3}{6\,(\hbar\bar{\omega})^3}\,, \tag{2.5}$$

where $\bar{\omega} = (\omega_x\omega_y\omega_z)$ is the geometric mean of the trapping frequencies. The density of states is related to $G(\varepsilon)$ through $g(\varepsilon) = dG/d\varepsilon$, so that one obtains

$$g_{ho}(\varepsilon) = \frac{\varepsilon^2}{2\,(\hbar\bar{\omega})^3}\,. \tag{2.6}$$

One should note that Eq. 2.6 assigns a weight of zero to the ground state. For a system with many identical fermions, this can be neglected as the ground state is occupied by one fermion at most, so that $N \approx N_{ex}$.

With the definitions above, the number of atoms N_{ex} in the excited states of a harmonic potential is given by

$$N_{ex} = \int_0^{\infty} n_{FD}(\varepsilon) g_{ho}(\varepsilon) d\varepsilon = \left(\frac{k_B T}{\hbar\bar{\omega}}\right) f_3(\tilde{z}) \quad \text{with} \quad \tilde{z} = e^{\beta\mu}\,, \tag{2.7}$$

where the so called fugacity $\tilde{z}$ has been introduced, and the polylogarithm function[1] $f_\nu(z)$ (also called the Fermi-Dirac function) is defined for positive integer and half integer values of ν by [49]

$$f_\nu(z) = \frac{1}{\Gamma(\nu)} \int_0^{\infty} \frac{x^{\nu-1}}{e^x z^{-1} + 1} dx = \sum_{k=1}^{\infty} \frac{(-1)^{k+1} z^k}{k^\nu}\,. \tag{2.8}$$

Density distributions

In the experiment, most information is obtained from density distributions of clouds that are imaged either inside the trap or after a short time of flight following their release from the trap. In order to derive these density distributions, a semi-classical approach is taken. In the Thomas-Fermi approximation ([55, 56]) each particle is treated as a wave packet with definite position $\vec{r}$ and momentum $\vec{p}$, and one assumes that there is one such state per six-dimensional phase space volume h^3 where h is Planck's constant. Under typical experimental conditions, this is a good approximation. The corresponding phase space

[1] The polylogarithm function is implemented in most established computational software programs such as Mathematica. For further information on fast and accurate numerical calculations, see [22] and references therein.

density $\rho(\vec{r},\vec{p})$ can be determined by combining Eqs. 2.6 and 2.7 with the normalization condition

$$N = \int \rho(\vec{r},\vec{p})\, d\vec{r} d\vec{p}\,. \tag{2.9}$$

Once again, the approximation $N \approx N_{ex}$ is used, and one obtains the phase space density

$$\rho(\vec{r},\vec{p}) = \frac{1}{h^3} n_{FD}\left[\varepsilon_{cl}(\vec{r},\vec{p})\right] \frac{1}{e^{\beta(\varepsilon_{cl}-\mu)}+1}\,, \tag{2.10}$$

where $\varepsilon_{cl}(\vec{r},\vec{p}) = \vec{p}^2/2m + V_{ho}(\vec{r})$ denotes the energy of a single classical particle in a harmonic potential. lassical particle in a harmonic potential. The intra-trap distributions in position and momentum space can then be determined by integrating Eq. 2.10 over the respective complementary space. For the density distribution in position space, this leads to

$$n(\vec{r}) = \frac{1}{\lambda_{dB}} f_{3/2}\left(\tilde{z} e^{-\beta V_{ho}(\vec{r})}\right)\,, \tag{2.11}$$

where the thermal de Broglie wavelength has been introduced:

$$\lambda_{dB} = \frac{h}{\sqrt{2\pi m k_B T}} \tag{2.12}$$

The resulting density distribution in momentum space is

$$n(\vec{p}) = \frac{1}{\lambda_{dB}} \frac{1}{(m\bar{\omega})^3} f_{3/2}\left(e^{-\beta\frac{p^2}{2m}}\right)\,. \tag{2.13}$$

Note that $n(\vec{p})$ is isotropic, whereas $n(\vec{r})$ depends on the actual trapping potential.

If the cloud is not detected within the trap but rather following some time of flight (tof) after the trap is switched off, the initial momentum distribution is converted into a spatial density distribution by the ballistic expansion. The momentum distribution can, in principle, be directly measured in this way by taking the limit of long expansion times. For intermediate expansion times, however, the initial density distribution must also be taken into account. For a harmonic potential, the semi-classical approximation yields the following density distribution after arbitrary times of flight [22]

$$\begin{aligned} n_{tof}(\vec{r},t) &= \int \rho(\vec{r}_0,\vec{p})\, \delta^3\left(\vec{r} - \vec{r}_0 - \frac{\vec{p}t}{m}\right) d^3\vec{r}_0 d^3\vec{p} \\ &= \frac{\prod_i \eta_i(t)}{\lambda_{dB}^3} f_{3/2}\left(\tilde{z} e^{-\frac{m}{2k_B T}\sum_i [\omega_i r_i \eta_i(t)]^2}\right) \end{aligned} \tag{2.14}$$

which is simply a rescaling of the coordinates by the factor

$$\eta_i(t) = \left[1+\omega_i^2 t^2\right]^{-1/2}\,. \tag{2.15}$$

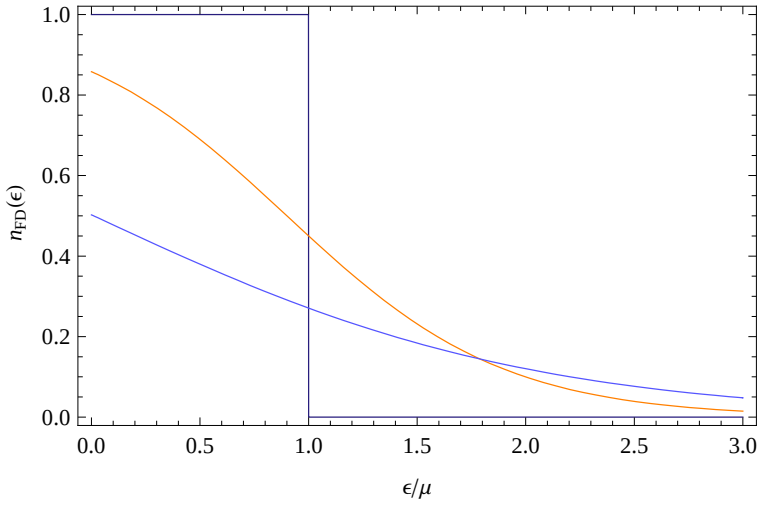

Figure 2.1: Fermi-Dirac statistics. The plot qualitatively shows the occupation probability at zero temperature (blue) and at increasing temperatures (orange and light blue).

The Fermi energy

In order to derive a relation that proves very useful in the thermometry of fermionic gases, we now consider the limit of very low temperatures $T \to 0$. It was pointed out above that in a system of identical fermions, any state can be occupied by at most one particle. At $T = 0$, therefore, all energy levels up to the the so-called Fermi energy $E_F = \mu\,(T \to 0, N)$ will be filled, $n_{FD}\,(\varepsilon \leq E_F) = 1$, while those levels with energies higher than E_F will be empty, $n_{FD}\,(\varepsilon > E_F) = 0$. The occupation probability can then be expressed by

$$n_{FD}\,(\varepsilon, T = 0) = \Theta\,(E_F - \varepsilon)\ , \tag{2.16}$$

where Θ is the Heaviside step function. The temperature corresponding to the Fermi energy, $T_F = E_F/k_B$, is called the Fermi temperature. In Fig. 2.1 the occupation probability $n_{FD}\,(\varepsilon)$ is plotted for several values of T. With increasing temperature, the step in $n_{FD}\,(\varepsilon)$ gradually broadens with a width on the order of $E_F \cdot T/T_F$. At temperatures $T \gg T_F$, the occupation probability $n_{FD}\,(\varepsilon) \ll 1$ for all energy levels, so that the gas behaves like a classical Maxwell-Boltzmann gas where the indistinguishability of the particles is not of importance. Thus, the Fermi energy marks the onset of quantum behavior of the gas.

Making use of Eq. 2.16 and 2.6 in the evaluation of Eq. 2.7 for $T = 0$ leads to a very simple expression for the Fermi energy in a harmonic potential:

$$N = \int_0^\infty n_{FD}(\varepsilon) g(\varepsilon) d\varepsilon = \int_0^{E_F} g(\varepsilon) d\varepsilon = \frac{E_F^3}{6(\hbar\bar{\omega})^3}\ . \tag{2.17}$$

Solving for E_F, we obtain

$$E_F = \hbar\bar{\omega}(6N)^{1/3}\ . \tag{2.18}$$

Combined with equation 2.7 this gives a useful, universal relation which is often used for estimates in the experiment:

$$\frac{T}{T_F} = \left[\frac{1}{6f_3(\tilde{z})}\right]^{1/3} \tag{2.19}$$

2.1.2 The ideal classical gas

If considered in the classical limit, $\tilde{z} = e^{\beta\mu} \ll 1$, the density and momentum distributions derived from Eq. 2.10 are reduce to those of a Maxwell-Boltzmann gas. In the case of a harmonic trapping potential, the expressions are Gaussian, and Eqs. 2.11 and 2.13 reduce to

$$n(\vec{r}) = \left(\frac{1}{\pi}\right)^{3/2} \frac{N}{\sigma_x\sigma_y\sigma_z} e^{-\sum_i \frac{x_i^2}{\sigma_i^2}} \tag{2.20}$$

$$n(\vec{p}) = \left(\frac{1}{\pi}\right)^{3/2} \frac{N}{\kappa^3} e^{-\sum_i \frac{p_i^2}{\kappa_i^2}}, \tag{2.21}$$

where $\sigma_i = [2k_BT/m\omega_i^2]^{1/2}$ and $\kappa = [2k_BTm]^{1/2}$ are the respective $1/e^2$ widths of the distributions. In a time-of-flight expansion, the momentum distribution remains unchanged and one obtains the evolution of the spatial density distribution by rescaling the waists according to $\sigma_i(t) = \sigma_i\eta_i(t)$ with $\eta_i(t)$ as defined above in Eq. 2.15.

2.2 Ultracold collisions

Collisions between particles can be either elastic or inelastic. Here I will focus on elastic collision processes, since they are essential for the relaxation process studied in this thesis. In the following, the concept of partial waves will be introduced, providing an elegant and very useful way to treat elastic collisions in the the low-temperature limit.

Inelastic collisions have their origin in the internal degrees of freedom of the atoms. For the right choice of atomic states in multi-species mixtures, spin-exchange collisions and dipolar relaxation are forbidden by selection rules or energetically suppressed at low temperatures. Further information on inelastic processes with regard to the mixture used in our experiment can be found in Ref. [22]. The reader interested in more details of scattering theory in general is referred to the literature [46, 57, 47].

2.2.1 Elastic collisions

The physical description of an elastic scattering process between two distinguishable particles with masses m_1 and m_2 can be separated into center-of-mass and relative coordinates, where the center-of-mass motion is conserved. The motion of the two particles relative to each other is equivalent to the scattering of one particle with reduced mass $\mu = m_1m_2/(m_1 + m_2)$ off the interatomic interaction potential $V_{sc}(\vec{r})$.

In an elastic collision the energy is an integral of the motion which allows the scattering problem to be formulated in a time-independent form. Indexing energy eigenstates by k, the corresponding stationary Schrödinger equation reads

$$\left[-\frac{\hbar^2\nabla^2}{2\mu}+V_{sc}\left(\vec{r}\right)\right]\psi_k\left(\vec{r}\right)=E\psi_k\left(\vec{r}\right)\ . \tag{2.22}$$

For distances r much larger than the range of the interaction potential, one can construct asymptotic solutions to Eq. 2.22 that are of the form [58]

$$\psi_k\left(\vec{r}\right)=C\left(e^{ik\vec{r}}+f\left(k,\theta,\phi\right)\frac{e^{ikr}}{r}\right)\qquad\text{for } r\to\infty\ . \tag{2.23}$$

Here the first term on the right hand side corresponds to an incoming plane wave with wave vector $\vec{k}$ and energy $E=\hbar^2k^2/2\mu$, and the second term (which falls off radially like a spherical wave) represents the scattered wave. C is a normalization constant and r,θ,ϕ are spherical coordinates. The so-called scattering amplitude $f\left(k,\theta,\phi\right)$ connects the wave function with the measurable quantities of the differential and total scattering cross sections,

$$\frac{d\sigma}{d\Omega}=\left|f\left(k,\theta,\phi\right)\right|^2\qquad\text{and}\qquad\sigma(k)=\int_\Omega\left|f\left(k,\theta,\phi\right)\right|^2d\Omega\ , \tag{2.24}$$

where $d\Omega=\sin\theta d\theta d\phi$ is the differential solid angle. For most potentials, the scattering problem cannot be solved analytically; in the case of a spherically symmetric potential V_{sc}, however, one important simplification can be made. There one can separate out the radial part of the solution function $\psi_k\left(\vec{r}\right)$, which allows $\psi\left(r,\theta,\phi\right)$ to be expanded in terms of spherical harmonics $Y_l^{m_l}\left(\theta,\phi\right)$, where l and m_l are quantum numbers for the total angular momentum and its projection onto the z-axis respectively:

$$\psi_k\left(\vec{r}\right)=\sum_{l,m_l}\frac{R_{k,l}(r)}{r}Y_l^{m_l}\left(\theta,\phi\right) \tag{2.25}$$

Contributions with the angular momentum quantum numbers $l=0,1,2$ are commonly referred to as s-, p-, and d-waves. Choosing the z-axis collinear with $\vec{k}$ leads to yet another simplification as the problem then becomes independent of the azimuthal angle ϕ, which means that only terms with $m_l=0$ contribute to Eq. 2.25. The scattering problem is thereby reduced to the solution of the radial Schrödinger equation

$$\left[-\frac{\hbar^2}{2\mu}\frac{d^2}{dr^2}+\frac{\hbar^2l(l+1)}{2\mu r^2}+V_{sc}(r)\right]R_{k,l}(r)=ER_{k,l}(r), \tag{2.26}$$

where the centrifugal barrier appears in addition to the scattering potential $V_{sc}(r)$. If $V_{sc}(r)$ is known, the Schrödinger equation can be solved numerically. With Eq. 2.23 and the use of some standard angular momentum algebra, the radial part of the asymptotic wave function can be written

$$R_{k,l}(r)\propto\left((-1)^{l+1}e^{-ikr}+e^{2i\delta_l}e^{ikr}\right) \tag{2.27}$$

where phase shifts δ_l (defined modulo π) are introduced. The effect of the scattering potential $V_{sc}(r)$ is therefore simply to produce a dephasing between incoming and outgoing partial waves. Once these scattering phases are calculated, one obtains the scattering amplitude from the relation

$$f(k,\theta) = \frac{1}{2ik}\sum_{l=0}^{\infty}(2l+1)\,P_l(\cos\theta)\left(e^{2i\delta_l(k)}-1\right). \tag{2.28}$$

Here P_l are Legendre polynomials. The total scattering cross section $\sigma(k)$ can be determined by inserting Eq. 2.28 into Eq. 2.24 and making use of the orthogonality relation of the Legendre polynomials, which yields

$$\sigma(k) = \sum_{l=0}^{\infty}\sigma_l(k) = \frac{4\pi}{k^2}\sum_{l=0}^{\infty}(2l+1)\sin^2(\delta_l). \tag{2.29}$$

The total scattering cross section is thus given by a sum over the partial wave contributions. The contribution of each partial cross section to the total scattering cross section has a maximum of $\sigma_{l,max} = 4\pi\,(2l+1)\,/k^2$ which is called the unitarity limit [46].

2.2.2 Elastic collisions at low energies

There is one very important consequence of the centrifugal barrier that appears in Eq. 2.26. If a partial wave has a collision energy which is much lower than the height of the barrier, it will only probe the slowly varying and weak outer part of the scattering potential and thus experience no significant phase shift. Scattering of partial waves with $l \geq 1$ is therefore suppressed for sufficiently low energies. For the scattering phase δ_l (modulo π) one finds that ([58])

$$\delta_l \propto k^{2l+1} \qquad \text{for} \qquad k \to 0\,. \tag{2.30}$$

Therefore the contribution of the partial waves to the total scattering cross section scales as

$$\sigma_l = \frac{4\pi}{k^2}\sin^2(\delta_l) \propto k^{4l} \propto E^{2l} \qquad \text{for} \qquad k \to 0 \tag{2.31}$$

which is known as the Wigner threshold law ([59]). This means that for collision energies much smaller than the height of the p-wave centrifugal barrier, only s-waves contribute to the scattering process. In that case, the effect of the scattering potential on the phase δ_0 can be described by a single parameter. This parameter is known as the s-wave scattering length a, and is defined by

$$a = -\lim_{k\to 0}\frac{\tan\delta_0(k)}{k}\,. \tag{2.32}$$

In case of distinguishable particles, the total scattering cross section is related to the scattering length by

$$\lim_{k\to 0}\sigma_{l=0}(k) = 4\pi a^2 \qquad \text{(distinguishable particles)}. \tag{2.33}$$

If the particles are identical, however, one cannot distinguish the scattering processes corresponding to $f(k,\theta)$ and $f(k,\pi-\theta)$. The scattering state must therefore be (anti-) symmetrized accordingly. For bosons, the interference of the two terms leads partial-wave contributions to the total scattering cross section that double for partial waves with even values of l and cancel for odd values of l. For fermions, the contributions cancel for even l and double for odd l. Thus, the total scattering cross sections in the s-wave limit are given by

$$\lim_{k\to 0}\sigma_{l=0}(k) = 8\pi a^2 \quad \text{(identical bosons)} \tag{2.34}$$

$$\lim_{k\to 0}\sigma_{l=0}(k) = 0 \quad \text{(identical fermions)} \tag{2.35}$$

for scattering between two identical bosons or two identical fermions, respectively.

A spin-polarized, single-species gas of fermionic atoms at low temperature is therefore well described as an ideal quantum gas since there are no s-wave interactions and contributions from higher order partial waves ($l = 1, 3, \dots$) are strongly suppressed. This is essential for the theoretical model of cross-dimensional relaxation and the corresponding experiment described in the following chapters.

The long-range part of the actual interaction potential of neutral atoms is usually very well approximated by the van der Waals interaction $V_{vdW} = C_6/r^6$, where the coefficient C_6 describes the strength of the interaction. Values of C_6 can be found in the literature for many species of interest ([60, 61, 62]). Using the long-range part of this potential allows the height $E_{th}(l)$ of the centrifugal barrier to be estimated by evaluating the effective potential of Eq. 2.26 (the sum of the centrifugal potential and the interaction potential) at its local maximum at $r > 0$. This yields

$$E_{th}(l) = 2\left[\frac{\hbar^2 l(l+1)}{6\mu}\right]^{3/2} C_6^{-1/2}\,. \tag{2.36}$$

For the fermionic species used in our experiment, we obtain threshold energies $E_{th,p}^{Li,Li} = 8m\mathrm{K}\times k_B$ for intra-species p-wave collisions of ^{6}Li and $E_{th,p}^{K,K} = 280\mu\mathrm{K}\times k_B$ for intra-species p-wave collisions of ^{40}K [22]. The p-wave threshold for collisions between lithium and potassium is $E_{th}^{Li,K} = 2.7\ \mathrm{mK}\times k_B$.

2.3 Optical dipole trap

For the experimental realization of cross-dimensional relaxation described in Chap. 4, the atoms were trapped in an optical dipole trap (ODT). This section presents the theoretical concepts of optical dipole trapping and provides equations that will be needed later on in this thesis.

In subsection 2.3.1 a formula will be derived that allows the intensity distribution of a Gaussian beam to be calculated. The physical mechanisms of optical dipole trapping are outlined in subsection 2.3.2, where formulas for the trap depth and the heating rate are

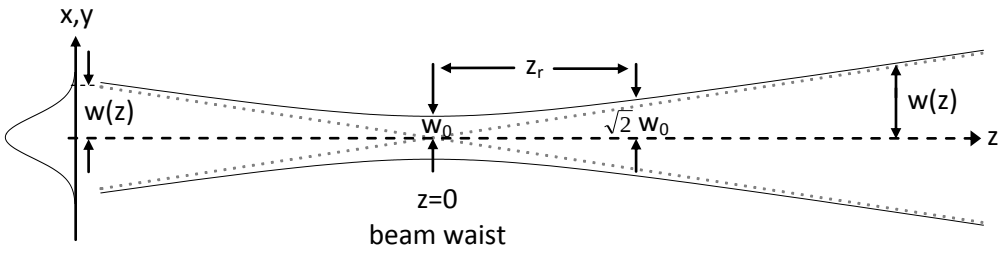

Figure 2.2: Gaussian beam: The propagation axis z is depticted horizontally, the radial axes vertically. An intensity profile is shown on the left.

provided. Subsection 2.3.3 discusses the trapping frequencies and provides an estimate of the extent of the harmonic region of the trap.

2.3.1 Intensity distribution of Gaussian beams

Laser beams are well described by the so-called paraxial wave equation[2]

$$\left(\nabla_T^2 + 2ik\partial_z\right) E_0 \approx 0 \text{ with } \nabla_T^2 = \partial_x^2 + \partial_y^2 \tag{2.37}$$

where E_0 is the amplitude of the electric field of an electro-magnetic wave propagating along the z-axis $E(\vec{r}) = E_0(\vec{r})e^{i\vec{k}\vec{z}}$, and the wave vector k is given by the dispersion relation $k^2 = \omega^2/c^2$. This equation is analogous to a two-dimensional Schrödinger equation in free space with t replaced by z. One can find solutions to this equation that are of the form

$$E_0(\vec{r}) \propto \frac{1}{\sqrt{1 + z^2/z_r^2}} e^{-i\varphi(z)} \exp\left(\frac{ik\left(x^2+y^2\right)}{2\left(z + z_r^2/z\right)} - \frac{x^2+y^2}{w^2(z)}\right) \tag{2.38}$$

with $w(z) = w_0\sqrt{1 + z^2/z_r^2}$, and $z_r = \pi w_0^2/\lambda$. The resulting intensity distribution

$$I(\vec{r}) \propto \left|E(\vec{r})\right|^2 \propto \frac{1}{1 + z^2/z_r^2} e^{-2(x^2+y^2)/w^2(z)} \tag{2.39}$$

is Gaussian and describes the beam profiles observed for real laser sources very well. Here $w(z)$ is a measure of the radial width of the beam, and z_r is the so-called Rayleigh range, defined as the distance along the beam propagation direction from the waist to the point where the cross-sectional area is doubled (see Fig. 2.2). The geometry of the beam propagating along the z-axis is therefore completely defined by the waist w_0 and either z_r or λ.

In order to obtain absolute values for the intensity at any point of the propagation axis, the normalization constraint $P \stackrel{!}{=} \int I(\vec{r})dxdy$ is used, which relates the total power

[2]The paraxial wave equation is a solution to the Helmholtz equation, which is obtained by a separation of the space- and time-dependence in the wave equation for the electric field. For a detailed derivation see e.g. [63]

P to the integral of the intensity I over a plane perpendicular to the propagation axis z. Separation of the beam waist w_0 into its x and y components yields

$$I(\vec{r}) = 2 \cdot \frac{P}{w^2(z)\pi} \exp\left(-\frac{2}{1+z^2/z_r^2}\left(\frac{x^2}{w_{0x}^2}+\frac{y^2}{w_{0y}^2}\right)\right) \quad \text{with} \tag{2.40}$$

$$z_r = \frac{w_{0x}w_{0y}\pi}{\lambda} \ , \ w_{x,y}(z) = w_{0x,0y}\sqrt{1+z^2/z_r^2} \ , \text{ and } \ w^2(z) = w_{0x}w_{0y}(1+z^2/z_r^2) \ . \tag{2.41}$$

Thus, the parameters that determine the intensity of the beam at a given point in space $\vec{r} = (x, y, z)$ are the wavelength λ, the total beam power P, and the respective beam waists w_{0x}, w_{0y} (centered around $\vec{r} = 0$) which are defined by that radial distance from the axis $r(x, y, z = 0)$ at which the intensity has decreased by a factor of $1/e^2$. In the general case of different beam waists in the different directions, w_z is the geometric mean of $w_x(z)$ and $w_y(z)$.

2.3.2 Optical dipole trap details

Optical dipole trapping relies on the electric dipole interaction of atoms with intense light which is detuned far from resonance with the nearest optical transition of the atoms. Due to the far detuning the optical excitation can be kept extremely low, which provides an advantage over traps based on radiation pressure (e.g. magneto-optical traps [64]) where the minimum attainable temperatures are limited by the photon recoil and the achievable density is limited by light-assisted inelastic collisions [65]. In addition, the trapping mechanism of optical dipole traps (ODTs) is largely independent of the particular magnetic sub-levels of the confined atoms, in contrast with magnetic traps ([66, 67]) that can only capture and confine so-called low field seeking internal states.

Red-detuned light – i.e., light with a wavelength longer than that corresponding to the nearest atomic transition – results in a negative interaction energy, which draws the atoms towards areas of stronger electric fields and thus higher intensities. Because of its conservative character, this force can be derived from a potential which is, as will be shown below, proportional to the light intensity I. The simplest implementation of an optical dipole trap is therefore a focused Gaussian laser beam with wavelength longer than the nearest optical transition. Since the intensity gradient and thus the confinement along the propagation axis z of the beam are considerably weaker than in the directions perpendicular to z, our experiment uses a *crossed* ODT consisting of two beams with overlapping foci, where the confinement is similar in all directions. Much of the treatment below is based on the comprehensive review article of Ref. [68].

Oscillator model

In order to derive the basic equations for the optical dipole potential and the scattering rate, one can consider the atom as a simple oscillator subject to a classical radiation field. The electric field $\vec{E}$ induces an atomic dipole moment $\vec{p}$ which oscillates at the driving

frequency ω. The amplitude p of this dipole moment is related to the field amplitude E by a complex polarizability $\alpha(\omega)$:

$$p = \alpha(\omega)E. \tag{2.42}$$

The real part of $\alpha(\omega)$ describes the in-phase component of the dipole oscillation which is responsible for the dispersive properties of the interaction. The interaction potential of the induced dipole moment $\vec{p}$ in the driving field $\vec{E}$ is thus given by

$$U_{dip} = -\frac{1}{2}\left\langle \vec{p}\vec{E} \right\rangle = -\frac{1}{2\varepsilon_0 c}\Re\left(\alpha(\omega)\right) I, \tag{2.43}$$

which is proportional to the field intensity $I = 2\varepsilon_0 c\,|E|^2$. Here the angular brackets $\langle\cdot\rangle$ denote the time average over the rapid oscillating terms, and the factor $\frac{1}{2}$ expresses the fact that the dipole moment is an induced, not a permanent one.

The imaginary part of $\alpha(\omega)$ describes the out-of-phase component of the dipole oscillation and allows the power that is absorbed by the oscillator from the driving field to be calculated:

$$P_{abs} = \left\langle \dot{\vec{p}}\vec{E} \right\rangle = 2\omega\Im(pE^*) = \frac{\omega}{\varepsilon_0 c}\Im\left(\alpha(\omega)\right) I. \tag{2.44}$$

When interpreted as scattered – i.e. absorbed and spontaneously re-emitted photons – P_{abs} can be used to determine the corresponding scattering rate

$$\Gamma_{sc}(\vec{r}) = \frac{P_{abs}}{\hbar\omega} = \frac{1}{\hbar\varepsilon_0 c}\Im\left(\alpha(\omega)\right) I(\vec{r}). \tag{2.45}$$

Using a simple, classical model one can calculate the polarizability α of an atom. There an electron with mass m_e is considered to be bound elastically to the core of the atom with an oscillation eigenfrequency ω_a that corresponds to the optical transition frequency of the atoms. As an accelerated charge, the oscillating electron emits dipole radiation, which results in a damping of the oscillation according to Larmor's formula (see, e.g. Ref. [69]). The polarizability is then calculated by integration of the equation of motion for the driven oscillation of the electron, yielding

$$\alpha = 6\pi\varepsilon_0 c^3 \frac{\Gamma/\omega_a^2}{\omega_a^2 - \omega^2 - \imath(\omega^3/\omega_a^2)\Gamma} \tag{2.46}$$

with a damping rate $\Gamma = e^2\omega_a^2/6\pi\varepsilon_0 m_e c^3$ due to the energy loss via radiation at resonance frequency ω_a.

Combining the formulas above yields the following explicit expressions for the dipole potential U_{dip} and the scattering rate Γ_{sc} in the relevant case of large detunings and insignificant saturation of the upper level:

$$U_{dip}(\vec{r}) = -\frac{3\pi c^2}{2\omega_0^3}\left(\frac{\Gamma}{\omega_a - \omega} + \frac{\Gamma}{\omega_a + \omega}\right) I(\vec{r}) \tag{2.47}$$

$$\Gamma_{sc}(\vec{r}) = \frac{3\pi c^2}{2\hbar\omega_a^3}\left(\frac{\omega}{\omega_a}\right)^3\left(\frac{\Gamma}{\omega_a - \omega} + \frac{\Gamma}{\omega_a + \omega}\right)^2 I(\vec{r}) \tag{2.48}$$

It is important to note that for detunings much smaller than the transition frequency $\Delta = \omega_a - \omega \ll \omega_a$ the dipole potential scales as I/Δ, whereas the scattering rate scales as I/Δ^2. For an increase in detuning the heating due to scattering will therefore decrease more rapidly than the laser power requirements increase.

In order to determine the trapping potential of a linear dipole trap, the intensity distribution of a Gaussian beam (Eq. 2.40) is substituted for $I(\vec{r})$ in Eq. 2.47. In general, potentials are additive, so the trapping potential of a crossed ODT of several laser beams can be calculated by simply summing over the individual potentials $U_{dip,crossed} = U_{dip,1} + U_{dip,2}(+\dots)$. This does not account for possible interference between the beams, but is a valid approximation if the beams have slightly different frequencies, such that the resulting lattice modulation oscillates much faster than the trapping frequencies. In the experiment, this frequency shift between beams is realized by acousto-optic modulators (AOMs)[3].

Photon recoil heating

The most prominent and limiting heating mechanism of atoms in ODTs is heating due to the spontaneous scattering of trap photons.

On absorbing and re-emitting a photon, an atom experiences a change in its kinetic energy due to the conservation of momentum. This change in energy in either of the processes, absorption and emission, can be quantified by considering the photon momentum, leading to an expression for the so-called recoil energy E_{rec} and a corresponding recoil temperature T_{rec}

$$E_{rec} = \frac{\hbar^2 k^2}{2m} = \frac{\hbar^2}{2m}\left(\frac{2\pi}{\lambda_a}\right)^2 = \frac{1}{2}k_B T_{rec}\,, \tag{2.49}$$

where $\lambda_a = 2\pi c/\omega_a$ is the wave length of the atomic transition and k_B is Boltzmann's constant. The factor 1/2 denotes a degree of freedom (and makes T_{rec} consistent with the thermal energy considerations below).
One should note that the absorption of the photon occurs in the propagation direction of the light field and is thus anisotropic, while the direction of its re-emission is random. When this is taken into account, the overall heating corresponds to an increase of thermal energy by $2E_{rec}$ in a time $\bar{\Gamma}_{sc}^{-1}$, which allows a heating power to be defined:

$$P_{heat} = 2E_{rec}\bar{\Gamma}_{sc} = \dot{\bar{E}}_{thermal}\,. \tag{2.50}$$

Here $\bar{\Gamma}_{sc}$ is the average photon scattering rate per atom and $\bar{E}_{thermal}$ is the mean thermal energy per atom. In a harmonic potential, the mean energy per atom in thermal equilibrium is given by

$$\bar{E} = U_0 + \bar{E}_{kin} + \bar{E}_{pot} = U_0 + 2\cdot\frac{3}{2}k_B T = U_0 + 3k_B T\,, \tag{2.51}$$

where $U_0 = U_{dip}(0)$ is the trap depth and the offset of the potential energy has been chosen such that $E_{pot} = 0$ at U_0. Using this relation between mean energy and temperature,

[3] For details, see Ref. [70].

one can now express the heating power resulting from photon scattering as a heating rate describing the corresponding increase of temperature with time. Using 2.49 and 2.50, one finds

$$\dot{\bar{E}} = P_{heat} \Rightarrow \dot{T} = \frac{1}{3}\bar{\Gamma}_{sc} T_{rec} \,, \tag{2.52}$$

which allows the temperature increase with time to be calculated if the average scattering rate $\bar{\Gamma}_{sc}$ is known. In order to obtain an expression for $\bar{\Gamma}_{sc}$, it is helpful to compare the expressions for the dipole potential and the scattering rate given in Eqs. 2.47 and 2.48. This shows that Γ_{sc} can be expressed in terms of U_{dip} by

$$\Gamma_{sc}\left(\vec{r}\right) = -\frac{K}{\hbar} U_{dip}\left(\vec{r}\right) \qquad \text{with} \qquad K = \left(\frac{\omega}{\omega_a}\right)^3 \left(\frac{\Gamma}{\omega_a - \omega} + \frac{\Gamma}{\omega_a + \omega}\right) \,. \tag{2.53}$$

Since this expression holds for any choice of $\vec{r}$, it can be used to calculate the averages $\bar{\Gamma}_{sc}$ and $\bar{U}_{dip}$. Using that $\bar{U}_{dip} = U_0 + \bar{E}_{pot} = U_0 + \frac{3}{2}k_B T$ one is left with

$$\bar{\Gamma}_{sc} = -\frac{K}{\hbar}\left(U_0 + \frac{3}{2}k_B T\right) \,. \tag{2.54}$$

Combined with Eq. 2.52 this gives

$$\frac{\dot{T}}{T} = -\frac{\left(U_0 + \frac{3}{2}k_B T\right) T_{rec}}{3\hbar} \left(\frac{\omega}{\omega_a}\right)^3 \left(\frac{\Gamma}{\omega_a - \omega} + \frac{\Gamma}{\omega_a + \omega}\right) \,. \tag{2.55}$$

If the thermal energy of the atoms in the trap is small compared to the trap depth[4] $k_B T \ll |U_0|$, which is often the case in experiments, the temperature-dependent term in Eq. 2.55 can be neglected and the right hand side reduces to a constant heating rate due to scattered light.

2.3.3 Harmonic approximation

Knowledge of the trapping frequencies of atoms in an ODT is essential as they determine many physical properties of the system. The trapping frequency is the rate at which the atoms, if considered as classical particles, oscillate in the trap and is usually calculated by using a harmonic approximation, where the coefficients of a second order Taylor series expansion of the dipole potential U_{dip} around its minimum at $\vec{r} = 0$ are identified with those of a harmonic oscillator $U_{ho}(i) = \frac{1}{2}m\omega_i^2 i^2$ $(i = x, y, z)$. This yields

$$\omega_i = \sqrt{\frac{1}{m}\partial_i^2 U_{dip}(\vec{r} = 0)} \,, \qquad \nu_i = \frac{\omega_i}{2\pi}, \tag{2.56}$$

where m is the mass of the atom being trapped.

An estimate of the harmonic region of the trap can be obtained by comparing a higher order expansion of U_{dip} with the second order terms and assessing the region as harmonic

[4] Here the absolute value is used since $U_0 < 0$ for red-detuned traps.

if the deviation of the higher order terms is small (e.g. smaller than 20 % of the absolute value of U_{dip}).

Under the influence of the earth's gravitational potential, the atoms are shifted along the direction of the gravitational acceleration $\vec{g}$ ("gravitational sag"). For atoms confined in the harmonic region of the trapping potential, the gravitational sag is given by

$$\Delta z = -\frac{g}{\omega_z^2} \propto m \tag{2.57}$$

where ω_z denotes the angular trapping frequency of the atoms along the direction of $\vec{g}$.

Chapter 3

Cross-dimensional relaxation in Fermi-Fermi mixtures

This chapter presents theoretical work on the equilibration rate of non-degenerate Fermi-Fermi mixtures undergoing cross-dimensional rethermalization (CDR).

Section 3.1 introduces the basics of CDR and gives an account of the previous work done on single-species CDR of bosons, and on Bose-Fermi mixtures. In section 3.2 a classical kinetic model of rethermalization is developed for the case of Fermi-Fermi mixtures. This model allows estimates to be given of the time constants of the relaxation as a function of the masses and particle numbers of the fermions in the mixture. Section 3.3 addresses effects due to finite initial deviations from thermal equilibrium. Classical Monte Carlo simulations were performed over a wide range of parameters to test and verify the validity of the predictions of our model. Details of these simulations are given in section 3.4. Finally, in section 3.5 predictions of the parameter β that connects the collision rates and the relaxation rates are presented for a number of Fermi-Fermi mixtures of current or possible future experimental interest.

3.1 CDR in a nutshell

If a gas is prepared with different mean thermal energies in the different Cartesian directions, i.e. $E_x \neq E_y \neq E_z$, the gas will subsequently relax into thermal equilibrium. In a purely harmonic trap the only way for the gas to rethermalize is to spatially redistribute its energy through collisions between the atoms. We focus here on temperatures well below the p-wave threshold of the atoms, so that only s-wave collisions between distinguishable particles need to be considered, as collisions between identical particles are suppressed by the Pauli exclusion principle. In an elastic s-wave collision, the total energy and momenta of the colliding particles are conserved, while their relative motion is completely randomized. The isotropic nature of the scattering amplitude therefore leads to a uniform redistribution of kinetic energy between the different directions. On the other hand, the

potential energy of an atom can be considered to be, on average, equal to its kinetic energy immediately following the collision. This assumption is valid in the so-called "collisionless" regime, where the collision rate is small compared to the trapping frequencies[1].

In the simulations described in this chapter and in the experimental attempts detailed in chapter 4 parameters lying well within the collisionless regime were used in order to ensure accurate results. J. Goldwin determined that the onset of hydrodynamic behavior occurs when the mean collision rate $\langle \Gamma_{coll} \rangle = \langle n \sigma v_{rel} \rangle$ reaches the same order of magnitude as the trap frequencies $\langle \Gamma_{coll} \rangle \sim \omega_{trap}$ [45]. Typical values used in the Monte-Carlo simulations presented in the following are $\langle \Gamma_{coll} \rangle < 10^{-2} \omega_{trap}$.

A detailed analysis of single-species CDR in a gas of bosons shows that the relaxation has the form of an exponential decay, with a $1/e$ time constant proportional to the mean time between collisions $\tau = \Gamma_{coll}^{-1}$[39]:

$$\Gamma_{relax} = \frac{1}{\alpha} \langle n \rangle \, \sigma \, \langle v_{rel} \rangle \,, \tag{3.1}$$

where n is the number density of the gas, σ is the elastic collision cross section, and v_{rel} is the relative collision speed. The angular brackets $\langle \cdot \rangle$ denote thermal averaging[2]. Here energy-independent s-wave collisions and Boltzmann statistics are assumed, so that the mean collision rate can be written $\Gamma_{coll} = \langle n \sigma v_{rel} \rangle = \langle n \rangle \, \sigma \, \langle v_{rel} \rangle$. The constant α, defined as the ratio of collision and relaxation rates, describes the average number of collisions per particle required for equilibration.

An extension to this model describing the rethermalization of a (spin-polarized) Bose-Fermi mixture reveals that the mean relaxation rate per fermion can be expressed in analogy with the single species case[71],

$$\Gamma_F = \frac{1}{\beta} \langle n_B \rangle_F \, \sigma_{BF} \, \langle v_{rel} \rangle \,. \tag{3.2}$$

Here $\langle n_B \rangle_F$ is the equilibrium density of the bosons, averaged over the fermion distribution; σ_{BF} is the inter-species elastic collision cross section; and $\langle v_{rel} \rangle$ is the relative collision speed between bosons and fermions. The constant of proportionality β reflects the mean number of collisions per fermion needed for rethermalization.

In a spin-polarized mixture of two fermionic species, only inter-species collisions contribute to the redistribution of energy. The relaxation is therefore again expected to re-

[1] This is in contrast to the hydrodynamic regime, where a particle undergoes many collisions within a time equal to the trap period. In this case, the atoms no longer undergo simple harmonic motion in the trap. The kinetic energy of the atoms is continually re-randomized by collisions, so that the gas will have an isotropic kinetic energy distribution while the potential (and center-of-mass kinetic) energies still retain the initial anisotropy. This results in a relaxation rate which is slower than that of the same system in the collisionless regime [45].

[2] The thermal average of a function $f(x,p)$ is obtained by summing over the values of $f(x,p)$ in all possible energy states the system can occupy: $(\sum_{x,p} Z)^{-1} \cdot \sum_{x,p} Z f(x,p)$ where $Z = Z(x,p)$ is the thermodynamic partition function. An in-depth treatment can be found in any textbook on thermodynamics and statistical mechanics, for instance Ref. [48, 49].

semble an exponential decay with a time constant for each species which is proportional to the mean time between inter-species collisions:

$$\begin{aligned} \Gamma_{F,1} &= \frac{1}{\beta_1} \langle n_2 \rangle_1 \sigma_{12} \langle v_{rel} \rangle , \\ \Gamma_{F,2} &= \frac{1}{\beta_2} \langle n_1 \rangle_2 \sigma_{12} \langle v_{rel} \rangle , \end{aligned} \tag{3.3}$$

where the terms on the right hand side are defined exactly as in Eq. 3.2.

For the type of relaxation treated here the gases have identical initial temperatures $T_x = \Omega_x T_z$, $T_y = \Omega_y T_z$, and T_z, with $\Omega_x, \Omega_y \neq 1$. Since the gases rethermalize together, they reach the same final temperature, which is given by $T_\infty = (\Omega_x + \Omega_y + 1)T_z/3$ in the classical gas limit. Therefore, there is no net transfer of energy between species during the relaxation. This fact is crucial for the validity of Eqs. 3.3.

3.2 Classical kinetic model

To better understand the physics of the rethermalization process, we now consider an analytic model for the relaxation. Here we closely follow the line of reasoning presented by Goldwin *et al.* in [45, 71], providing substantial extensions to the existing model. Firstly, the change from a Bose-Fermi to a Fermi-Fermi mixture allows estimates of the two constants of proportionality β_1 and β_2 to be made. Secondly, both Goldwin's theory and the corresponding experimental work [44] assume cylindrical symmetry of the initial energy anisotropy, i.e. $\frac{E_x}{E_z} = \frac{E_y}{E_z} = \Omega$. To allow a wider scope in the experiment, the generalized model also accounts for anisotropies with $\Omega_x \neq \Omega_y$.

The analysis is based on the Chapman-Enskog equation, which is equivalent to the Boltzmann transport equation [48]. According to this treatment, the rate of change of the ensemble average of any function of the two species' positions and velocities, usually denoted $\chi(\vec{x}_1, \vec{v}_1; \vec{x}_2, \vec{v}_2)$, is given by

$$\langle \dot{\chi} \rangle = \sigma \langle n v_{rel} \Delta\chi \rangle . \tag{3.4}$$

Once more the assumption of energy-independent s-wave scattering has been used to separate the collision cross section σ from the ensemble average. The quantity $\Delta\chi$ is the change in χ due to a single collision. We choose

$$\chi_1 \equiv E_{1,x} - E_{1,z}, \tag{3.5}$$

and consider fermions of type 1 colliding with fermions of type 2. The energy $E_{1,i}$ denotes the total (kinetic plus potential) energy of type-1 atoms in the ith direction. Note that due to our interest in χ_1 the ensemble average in Eq. 3.4 is taken only over the distribution

function for the type-1 fermions. Immediately after a collision, only the kinetic energy of the particles has changed, so that

$$\Delta\chi_1 = \Delta\left(E_{1,x}^{kin} - E_{1,z}^{kin}\right) = \frac{1}{2}m_1\Delta\left(v_{1,x}^2 - v_{1,z}^2\right). \tag{3.6}$$

As $\Delta\chi_1$ has no position dependence, the type-2 particle density n_2 can be removed from the average, yielding

$$\langle\dot{\chi}_1\rangle = \frac{1}{2}m_1\langle n_2\rangle\sigma_{12}\left\langle v_{rel}\Delta\left(v_{1,x}^2 - v_{1,z}^2\right)\right\rangle. \tag{3.7}$$

Defining the center-of-mass (c.m.) and relative velocities in the usual manner,

$$\begin{aligned}\vec{V}_{c.m.} &= \frac{m_1\vec{v}_1 + m_2\vec{v}_2}{m_1+m_2},\\ \vec{v}_{rel} &= \vec{v}_1 - \vec{v}_2,\end{aligned} \tag{3.8}$$

one can write

$$\begin{aligned}v_{1,x}^2 - v_{1,z}^2 = \left(V_{c.m.x}^2 - V_{c.m.z}^2\right) + \left(\frac{m_2}{m_1+m_2}\right)^2\left(v_{relx}^2 - v_{relz}^2\right)\\ +2\frac{m_2}{m_1+m_2}\left(V_{c.m.x}v_{relx} - V_{c.m.z}v_{relz}\right).\end{aligned} \tag{3.9}$$

Since the collision leaves $\vec{V}_{c.m.}$ and $|\vec{v}_{rel}|$ unchanged, but randomly rotates the direction of $\vec{v}_{rel}$, one is left with

$$\begin{aligned}\langle\dot{\chi}_1\rangle = -\frac{1}{2}\frac{m_1m_2}{(m_1+m_2)}\langle n_2\rangle\sigma_{12}\Bigg\langle v_{rel}\Bigg[\frac{m_2}{m_1+m_2}\left(v_{relx}^2 - v_{relz}^2\right)\\ +2(V_{c.m.x}v_{relx} - V_{c.m.z}v_{relz})\Bigg]\Bigg\rangle.\end{aligned} \tag{3.10}$$

Here only the quantities immediately before the collision need to be considered as there is no preferred direction of $\vec{v}_{rel}$ after the collision.

Calculating these ensemble averages for arbitrary masses and energy anisotropies – which are in general different between species at intermediate times of the relaxation process, compare figure 3.2 – is nontrivial, but some simple approximations may be used.

For the first terms one can easily show that for Boltzmann distributions in thermal equilibrium one has

$$\left\langle v_{rel}v_{reli}^2\right\rangle = \frac{4}{3}\langle v_{rel}\rangle\left\langle v_{reli}^2\right\rangle,\ i = x, z. \tag{3.11}$$

For the other terms it is important to note that $\langle V_{c.m.i}v_{reli}\rangle \neq 0$ for a gas with a cross-dimensional energy anisotropy (compare Eq. A.1). For cross terms of the form $\langle V_{c.m.i}v_{reli}\rangle$,

which vanish under equilibrium conditions, one can therefore still consider the limit of small deviations from thermal equilibrium. This yields a second approximation which is similar to the above result:

$$\langle v_{rel} V_{c.m.i} v_{reli} \rangle = \frac{4}{3} \langle v_{rel} \rangle \langle V_{c.m.i} v_{reli} \rangle . \tag{3.12}$$

Extensive numerical integrations of Gaussian distributions verified that these approximations are reasonable for small anisotropies. Since they would only serve as a distraction here, the details of these calculations and recommended limits for the anisotropies that should be considered in Monte Carlo simulations and experiments are presented in appendix A. Also contained in the appendix is a plot showing the evolution of the values of $\langle v_{rel} v_{reli}^2 \rangle$ over the course of a rethermalization process using realistic parameters, which gives an illustration of the validity of the approximations. Combining these results leads to

$$\begin{aligned} \langle \dot{\chi}_1 \rangle = -\frac{2}{3} \langle n_2 \rangle_1 \sigma_{12} \langle v_{rel} \rangle \frac{m_1 m_2}{m_1 + m_2} \Bigg\langle \frac{m_2}{m_1 + m_2} \left(v_{relx}^2 - v_{relz}^2 \right) \\ + 2 (V_{c.m.x} v_{relx} - V_{c.m.z} v_{relz}) \Bigg\rangle . \end{aligned} \tag{3.13}$$

Accounting for the fact that in the collisionless regime the mean kinetic and potential energies in a given direction are equal, one can now resubstitute for v_1 and v_2. Using $\langle v_{1i} v_{2i} \rangle = 0$, one finally obtains

$$\langle \dot{\chi}_1 \rangle = -\frac{2}{3} \langle \Gamma_{12} \rangle \frac{m_2}{(m_1 + m_2)^2} \langle (2m_1 + m_2) \chi_1 - m_1 \chi_2 \rangle . \tag{3.14}$$

Here the collision rate $\langle \Gamma_{12} \rangle = \langle n_2 \rangle_1 \sigma_{12} \langle v_{rel} \rangle$ describes the rate per type-1 particle of collisions with particles of type 2. Simply swapping $1 \leftrightarrow 2$ in Eq. 3.14 yields the time dependence of χ_2 which is defined in analogy with Eq. 3.5. Introducing dimensionless times $\tau_1 = \Gamma_{12} t$ and $\tau_2 = \Gamma_{21} t$, the final result is:

$$\begin{aligned} \frac{d}{d\tau_1} \langle \chi_1 \rangle &= -\frac{2}{3} \frac{m_2}{(m_1 + m_2)^2} \langle (2m_1 + m_2) \chi_1 - m_1 \chi_2 \rangle \\ \frac{d}{d\tau_2} \langle \chi_2 \rangle &= -\frac{2}{3} \frac{m_1}{(m_1 + m_2)^2} \langle (m_1 + 2m_2) \chi_2 - m_2 \chi_1 \rangle \end{aligned} \tag{3.15}$$

The solution of these coupled differential equations gives the time evolution of χ_1 and χ_2. Note that because of the definition of Γ_{12} (Γ_{21}), we are now in a position to not only consider mixtures of fermions with different masses but also to make predictions for the time evolution of mixtures with different atom numbers N_1 and N_2.

Introducing a normalized mass $\eta_1 = \frac{m_1}{m_1+m_2}$ ($\eta_2 = \frac{m_2}{m_1+m_2} = 1-\eta_1$), the solution of Eq. 3.15 can be expressed in terms of η_1 as

$$\chi_1(\tau_1) = \frac{(1-\eta_1)(1-2\eta_1)e^{-2\tau_1/3} + \eta_1 e^{-\frac{4}{3}\eta_1(1-\eta_1)\tau_1}}{1-2\eta_1(1-\eta_1)}. \tag{3.16}$$

Again the corresponding expression for χ_2 is obtained by simply swapping $1 \leftrightarrow 2$ in Eq. 3.16. The following steps are identical for χ_1 and χ_2, and so the indices will be dropped. β is determined by fitting a simple exponential decay to Eq. 3.16 and analytically minimizing the integrated squared error

$$\mathrm{err}^2 = \int_0^\infty \mathrm{d}\tau \left(\chi(\tau) - e^{-\frac{\tau}{\beta}}\right)^2 \tag{3.17}$$

with respect to the parameter β. Note that for reasons of simplicity $\chi(\tau = 0)$ is set to 1 without loss of generality. Minimizing requires $\frac{\partial}{\partial\beta}\mathrm{err}^2 = 0$, so one has to solve

$$0 = \int_0^\infty d\tau \left(\chi(\tau) - e^{-\frac{\tau}{\beta}}\right) \tau e^{-\frac{\tau}{\beta}}. \tag{3.18}$$

Carrying out this integral leads to a condition that relates β to η and hence the masses of the fermions in the mixture:

$$\frac{(1-2\eta)(1-\eta)}{(2\beta+3)^2} + \frac{\eta}{(4\eta(1-\eta)\beta+3)^2} = \frac{1}{36}(1-2\eta(1-\eta)). \tag{3.19}$$

This polynomial equation can be solved numerically with Mathematica's rootfinder. Convergence to the physical root can be ensured by using an initial value for β obtained from the small-time expansion of $\chi(\tau)$, which gives an estimate of $\beta = -\frac{3}{2(1-\eta)}$.

A theory curve plotting β as a function of η is shown in figure 3.1. The orange and blue points are results from Monte Carlo simulations which are described in detail in section 3.4. A list of values of β for the Li-K and a number of other mixtures can be found in section 3.5.

3.3 Effect of the finite size of the initial perturbation

The analysis presented thus far is limited to the case of small deviations from thermal equilibrium, and hence small initial energy anisotropies. In Monte Carlo simulations and experiments, however, large anisotropies are required for good signal-to-noise ratios. Thus understanding the effect of the finite departure from equilibrium is a necessary component of the analysis of the simulations as well as experimental measurements.

Eq. 3.3 followed the convention of Ref. [71] and defined the relaxation rate in terms of the final equilibrium collision rate. As pointed out in the same paper, one therefore has to account for the fact that the mean collision rate undergoes slight changes during the relaxation process as a consequence of the redistribution of energy[40]. Due to the

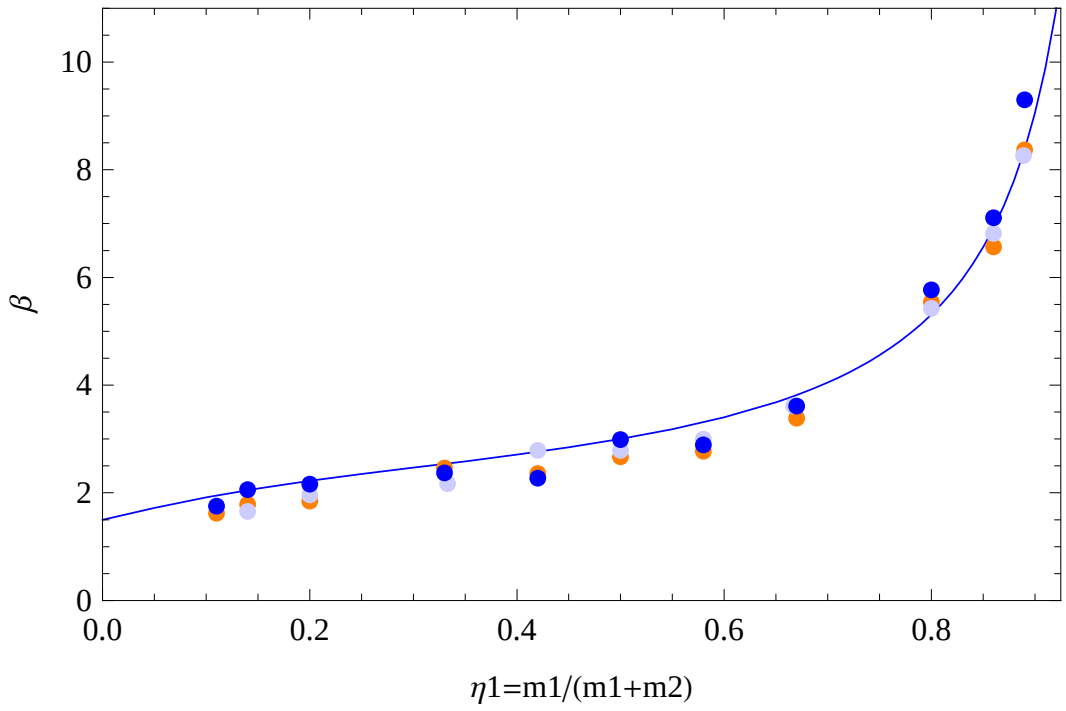

Figure 3.1: Number of collisions per fermion needed for rethermalization. The blue line indicates the theoretical prediction, while the orange, blue, and light blue points are results of Monte-Carlo simulations. For the blue points, equal particle numbers $N_1 = N_2$ for both species were assumed and the initial energy anisotropies were $\Omega_x = 2$ and $\Omega_y = 65$(blue) and $\Omega_x = 7$ and $\Omega_y = 4$ (light blue). The orange points were obtained from simulations with $N_1 = 2N_2$ and initial anisotropies $\Omega_x = 1.6$ and $\Omega_y = 1.3$.

exponential nature of the relaxation, the bulk of rethermalization occurs at initial times, so it is expected that the observed number of collisions needed for equilibration will be rescaled by a factor of approximately

$$\lambda(\Omega_x, \Omega_y) = \frac{\langle \Gamma_{coll}(t \to \infty) \rangle}{\langle \Gamma_{coll}(t = 0) \rangle}. \tag{3.20}$$

The function $\lambda(\Omega_x, \Omega_y)$ has a maximum of 1 for $\Omega_x = \Omega_y = 1$ and goes to zero as either Ω_x or Ω_y tend to 0 or ∞. In Ref. [71], an analytic expression for λ is derived under the assumption of cylindrical symmetry of the anisotropy. In the general case that is of interest here, λ can only be determined by means of numerical integration. This was done, for example, to rescale the results from the Monte Carlo simulations shown in Fig. 3.1; the points in this plot have been rescaled by a factor of $\lambda(\Omega_x, \Omega_y)^{-1}$.

3.4 Monte Carlo simulation

This section describes details of the Monte Carlo simulations that were used to test the model of section 3.2 and verify its predictions. Subsection 3.4.1 gives an outline of the simulations, while a more visual approach is taken in subsection 3.4.2, where the sequence of steps carried out in the simulation is presented in a flowchart. Subsection 3.4.3 discusses suitable parameter choices and some failure modes that were studied. Most of this section is based on the work of Refs. [71, 45]; differences are pointed out where relevant.

3.4.1 Outline

The simulation is started by preparing an ensemble consisting of N_1 type-1 and N_2 type-2 fermions in a harmonic trapping potential. This ensemble is initialized by assigning a random position and velocity vector to each particle from separable Gaussian distributions (equations 2.21). These distributions are scaled such that there is a factor of Ω_x or, respectively, Ω_y imbalance between the mean kinetic and potential energies per particle in the x and y dimensions with respect to the z dimension. The initial energy in a given dimension, however, is the same for both species. The positions and velocities of the particles are then evolved according to Newton's laws for some small time step Δt, before collisions are considered.

Since the Pauli exclusion principle forbids intra-species collisions in a system of spin-polarized fermions, only collisions of type-1 atoms with type-2 atoms are allowed. If two particles k and l are found within a critical distance r_c of each other, the pair is given a chance to collide. The collision probability is given by $p_{coll} = \sigma_{kl} v_{rel} \Delta t / V_c$, where σ_{kl} is the collisional cross section, $v_{rel} = |\vec{v}_k - \vec{v}_l|$ is the relative collision speed, and $V_c = \frac{4}{3} r_c^3 \pi$ is the volume of the sphere containing the colliding atoms. If p_{coll} is greater than a random number drawn from a uniform distribution on (0,1), an s-wave collision takes place and the relative velocity vector is rotated into a random direction (conserving the total momentum

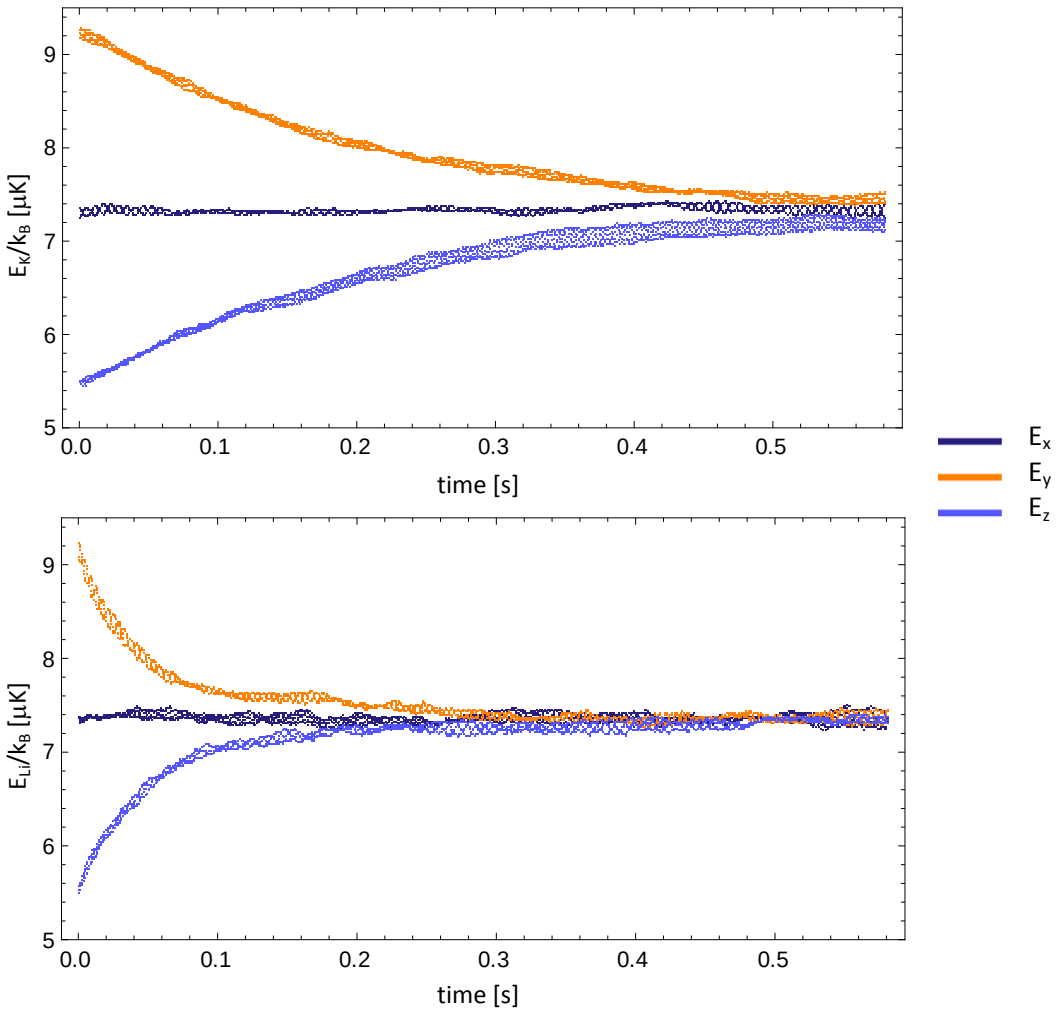

Figure 3.2: Typical relaxation curves of a Monte Carlo simulation of a Fermi-Fermi mixture of ^{40}K and ^{6}Li with initial anisotropies $\Omega_x = 1.33$ and $\Omega_y = 1.67$; the particle numbers N_K and N_{Li} were equal. The trapping frequencies (ν_x, ν_y, ν_z) were $(1140, 934, 654)$ Hz for potassium and $(1957, 1122, 1603)$ Hz for lithium. The trapping frequencies and the temperature correspond to realistic experimental conditions.

and energy). Finally, after all possible collision pairs have been considered, the mean energies of each species in each of the three Cartesian directions are recorded, and a new time step proceeds.

Typical relaxation curves obtained from a simulation with ^{40}K and ^{6}Li atoms are shown in figure 3.2. The parameters used in the simulation correspond to realistic parameters from our experiments, cf. chapter 4. As expected, the lighter lithium atoms relax quickly, while the heavier potassium atoms need a larger number of collisions to entirely redistribute their energy.

The relaxation rate Γ_σ of the energy anisotropy of species σ is determined by fitting the ratio of the energies in the respective directions to the ratio of decaying exponentials:

$$\frac{E_i}{E_j} = \frac{1 + \varepsilon_i \exp(-\Gamma_\sigma t)}{1 + \varepsilon_j \exp(-\Gamma_\sigma t)} \tag{3.21}$$

Here E_i (E_j) is the mean total energy per particle of the fermions in the i^{th} (j^{th}) direction, and we have defined[3]:

$$\begin{aligned} \varepsilon_x &= \frac{2\Omega_x - \Omega_y - 1}{\Omega_x + \Omega_y + 1} \\ \varepsilon_y &= \frac{2\Omega_y - \Omega_x - 1}{\Omega_x + \Omega_y + 1} \\ \varepsilon_z &= \frac{2 - \Omega_x - \Omega_y}{\Omega_x + \Omega_y + 1} \end{aligned} \tag{3.22}$$

In case of cylindrical symmetry ($\Omega_x = \Omega_y$), this fitting model reduces to the form presented in Ref. [71].

3.4.2 Flowchart of the Monte Carlo simulation

On pages 33–35, the structure and the individual steps of the Monte Carlo simulation outlined in the previous section are presented in a simplified flowchart. For clarity's sake, some output options are not shown in the flowchart but will instead be discussed in the text. These outputs can be used to double-check that the input parameters (such as collision probability and search volume) are processed correctly in the simulations.

Suitable choices for these parameters are discussed in the next section. In order to check the collision probability p_{coll}, the number N_p of possible collisions found in **Step 2**, and the number N_c of those collisions that actually take place (**Step 3**) are recorded for every iteration step. The collision probability is simply given by the ratio N_c/N_p. Proper evaluation of the search volume V_c can be checked for by recording the number N_d of double collisions found in **Step 2**, i.e. the number of incidents where more than two particles are found within V_c. As the density distribution in the trap is known, it is easy to calculate if V_c is processed correctly.

[3]Two assumptions are used to obtain these equations: the conservation of energy, and the isotropic nature and energy independence of s-wave collisions that allow the relaxation to be described by an ansatz of simple exponential decay $\Delta E_i(t) = \Delta E_i(0) e^{-\Gamma_F t}$ to describe the relaxation.

Generate initial distrbutions in the harmonic trap

Assign to each particle
random coordinates in the x-, y- and z-directions taken from Gaussian distributions

$$n(r_i) = \frac{1}{\sqrt{\pi}} \frac{1}{\sigma_i} \exp\left(-\frac{r_i^2}{\sigma_i^2} \right) \text{ with } i = x, y, z \text{ and } \sigma_i = \left(\frac{2k_B T_i}{m\omega_i^2} \right)^{\frac{1}{2}}$$

and random velocities in the x-,y- and z-direction also taken from Gaussian distributions

$$n(v_i) = \frac{1}{\sqrt{\pi}} \frac{1}{\kappa_i} \exp\left(-\frac{v_i^2}{\kappa_i^2} \right) \text{ with } i = x, y, z \text{ and } \kappa_i = \left(\frac{2k_B T}{m} \right)^{\frac{1}{2}}$$

Define goal number of iterations $i_{\max}$.
Set counter to $i = 1$.

Start simulation

Step 1

Evolve positions and velocities for time step Δt:

Determine total energy of each particle in a given direction $i = x, y, z$ and solve for maximum amplitude of the oscillation

$$r_{i,\max} = \sqrt{r_i^2 + \frac{v_i^2}{\omega_i^2}}$$

Determine phase φ_i of the oscillation in the trap

$$\varphi_i = \begin{cases} \arcsin\left(\frac{r_i}{r_{i,\max}} \right) \Leftrightarrow v_i > 0 \\ \pi - \arcsin\left(\frac{r_i}{r_{i,\max}} \right) \Leftrightarrow v_i < 0 \end{cases} \quad \text{or } \varphi_i = 0 \Leftrightarrow v_i = 0$$

Calculate and record new positions and velocities

$$r_{i,new} = r_{i,\max} \sin\left(\omega_i \Delta t + \varphi_i \right)$$

$$v_{i,new} = r_{i,\max} \omega_i \cos\left(\omega_i \Delta t + \varphi_i \right)$$

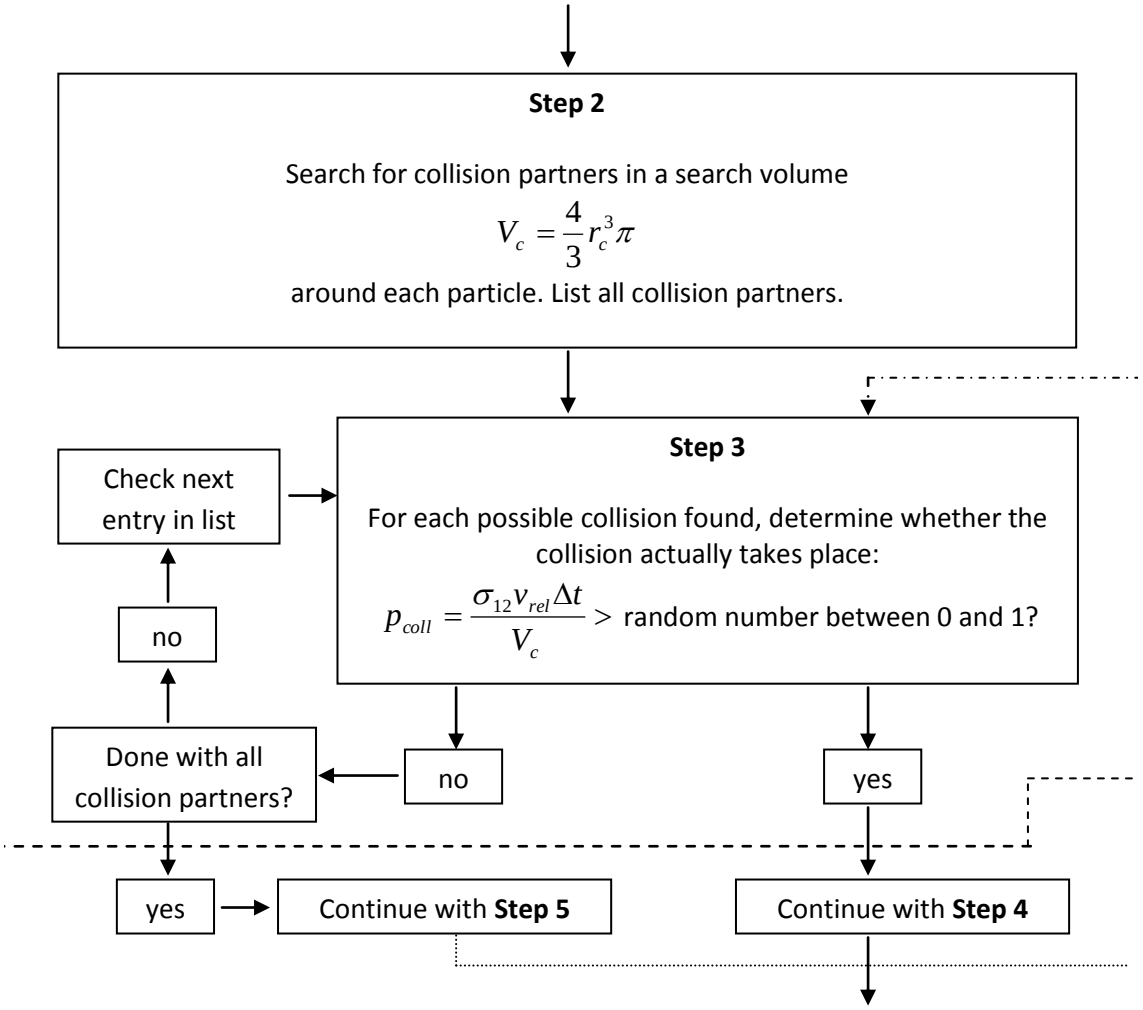

Step 4

For the particles k and l involved in the collision, calculate the new velocities:
Rotate the relative velocity vector $\vec{v}_{rel} = \vec{v}_1 - \vec{v}_2$ into a random direction

$$\vec{v}_{rel,new} = v_{rel} \cdot \begin{pmatrix} \sin\vartheta\cos\varphi \\ \sin\vartheta\sin\varphi \\ \cos\varphi \end{pmatrix},$$

where φ is a random number drawn from a uniform distribution between 0 and 2π, and ϑ is $\arccos(\xi)$ of a random number ξ from a uniform distribution between -1 and 1.
With the center-of-mass velocity

$$\vec{V}_{c.m.} = \frac{m_k \vec{v}_k + m_l \vec{v}_l}{m_k + m_l},$$

the velocities after the collision are given by

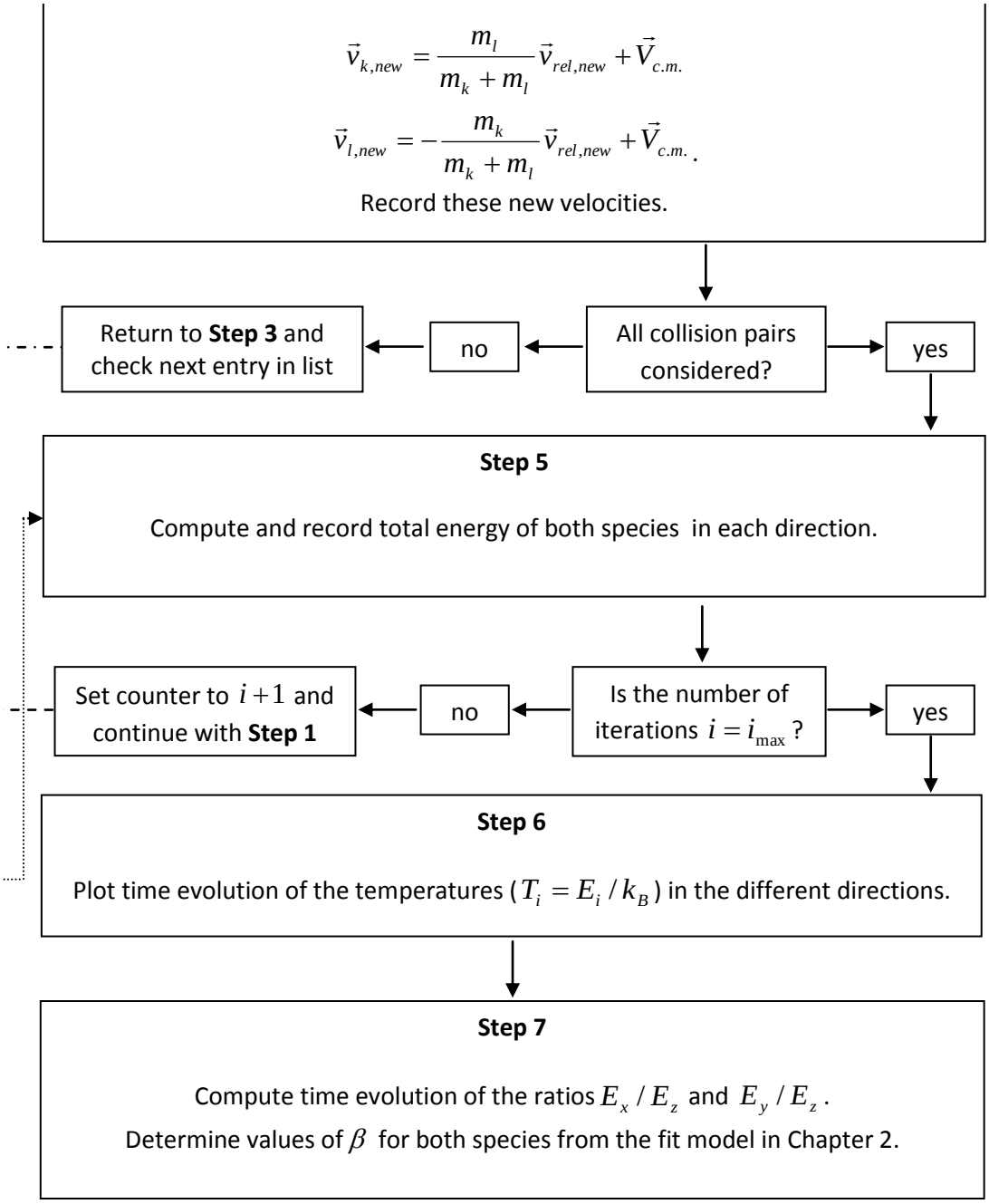
$\vec{v}_{k,new} = \frac{m_l}{m_k + m_l}\vec{v}_{rel,new} + \vec{V}_{c.m.}$
$\vec{v}_{l,new} = -\frac{m_k}{m_k + m_l}\vec{v}_{rel,new} + \vec{V}_{c.m.}$.
Record these new velocities.
All collision pairs considered?
yes
no
Return to **Step 3** and check next entry in list
Step 5
Compute and record total energy of both species in each direction.
Is the number of iterations $i = i_{\max}$?
yes
no
Set counter to $i+1$ and continue with **Step 1**
Step 6
Plot time evolution of the temperatures ($T_i = E_i / k_B$) in the different directions.
Step 7
Compute time evolution of the ratios E_x / E_z and E_y / E_z.
Determine values of β for both species from the fit model in Chapter 2.

3.4.3 Choice of parameters

Monte-Carlo simulations are a very useful tool for simulating a variety of experiments, but when first programming a new simulation, it turns out that this can be an experiment om itself. For the simulation to produce reliable and plausible results, it is essential to identify a suitable region of parameter space and to understand the effects of poorly-chosen parameters.

Collision probability

Following Ref. [71], the probability of two particles k and l colliding was taken to be

$$p_{coll} = \frac{\sigma_{kl} \left| \vec{v}_k - \vec{v}_l \right| \Delta t}{V_c}. \tag{3.23}$$

This, however, does not represent a probability in the conventional sense, because the equilibrium distribution of relative speeds is Gaussian, which means that for any given values of the collision cross-section, time step and search volume, there is some finite probability that the relative collision speed is large enough to make p_{coll} greater than one. The actual distribution of times between collisions is given by a Poisson distribution [72], so that the true collision probability is

$$\begin{aligned} P_{coll} &= 1 - \exp\left(-p_{coll}\right) \\ &\cong p_{coll} \qquad\qquad \text{for small } p_{coll} \end{aligned} \tag{3.24}$$

Therefore, p_{coll} should be kept well below 10% for accurate results, which is also recommended by Refs. [71] and [73]. Figure 3.3 depicts $(1 - \exp(-p_{coll}))$ (dashed) and p_{coll} (dotted) for comparison.

Since it ignores any possibility of either 3-body collisions or multiple 2-body collisions within a single time-step, Eq. 3.23 is still only approximate, but as it turns out it is still very good until exceedingly poor choices of the parameters Δt and r_c are made.

Time step

Figure 3.3 shows the number of collisions per calculated collision time $\langle \tau_{coll} \rangle = \langle \Gamma_{coll} \rangle^{-1}$ as a function of $\langle p_{coll} \rangle$ for a single-species simulation of (bosonic) particles in equilibrium. Here, V_c and $\langle v_{rel} \rangle$ are fixed to reasonable values, with Δt used as a scaling parameter. When $\langle p_{coll} \rangle$ becomes too large, an artificially lower number of collisions are observed than would be expected, since collisions are searched for only once per time-step. The results in figure 3.3 suggest that the approximation in Eq. 3.23 is still good for $\langle p_{coll} \rangle \sim 1$. The simulations presented here typically use $\langle p_{coll} \rangle$ in the range of 5×10^{-3} to 5×10^{-2} and are therefore expected to be accurate in this respect.

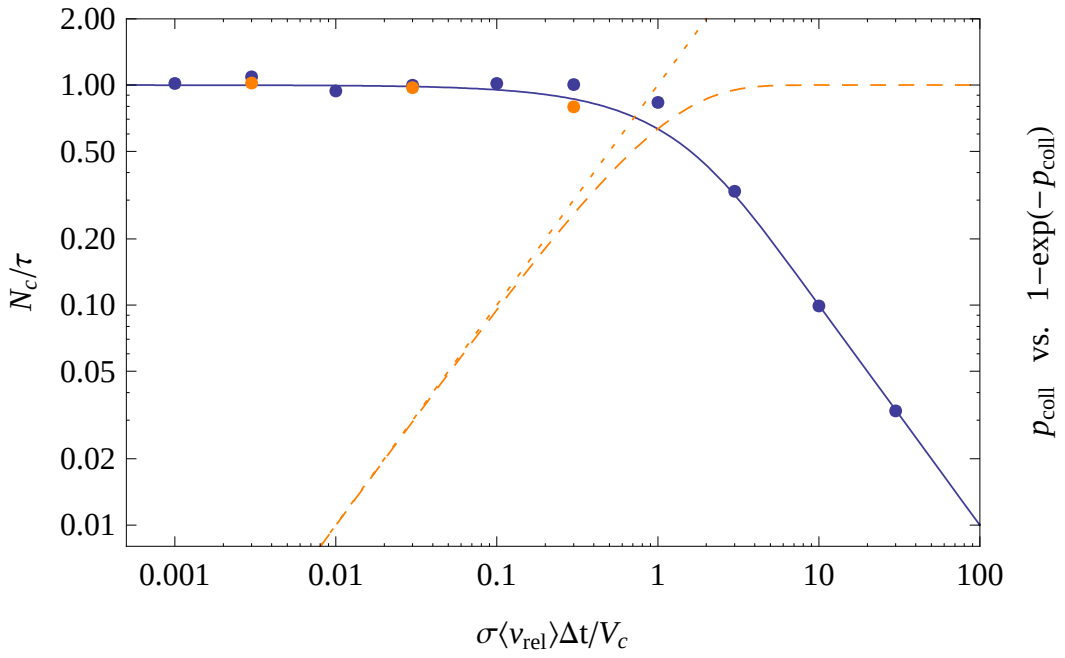

Figure 3.3: Effect of poor choice of time-step on the Monte-Carlo simulation. Plotted here is the number of collisions N_c per calculated collision time τ as a function of $\langle p_{coll}\rangle$ for a single-species gas of bosons in equilibrium. Blue points use p_{coll}, orange points use $1-\exp(-p_{coll})$ to calculate the collision probability in the simulations. The solid blue line illustrates the expected behavior for a Poisson distribution. The orange lines show p_{coll} (dotted) and $1-\exp(-p_{coll})$ (dashed), respectively. All simulations used 10^3 particles with an average of 10^{-2} particles per search volume V_c.

Search volume

Another input parameter that, if poorly chosen, can impair the correct outcome of a simulation is the search volume $V_c = \frac{4}{3} r_c^3 \pi$. Particles in the simulation must come within a critical distance r_c of each other for a collision to be considered. If V_c is large enough, any given particle will see all $N-1$ of the other particles within the volume, and the number of collisions per particle in one collision time will saturate at $(N-1)\langle p_{coll}\rangle$. On the other hand, every increase in V_c will also lead to an increase in Δt if $\langle p_{coll}\rangle$ is kept constant, so from some point on collisions will not be searched for often enough and the number of collisions per particle N_c and the collision time τ is expected to decrease.

Note that the approach taken here is different from Ref. [45]. To find an upper limit for V_c, let us look at the average number of collisions per particle within the collision time τ. N_c is determined by

$$N_c = N_{c,tot} \cdot \frac{\tau}{\Delta t} \cdot \frac{2}{N}, \tag{3.25}$$

where $N_{c,tot}$ is the total number of collisions detected within the time step Δt, and N is the number of particles in the simulation. There are always two particles involved in a collision, hence the division by $N/2$. The total number of collisions $N_{c,tot}$ is given by the number of collision partners N_p found in V_c multiplied by the collision probability p_{coll}. Using the definition of Eq. 3.23, this leads to

$$\begin{aligned} N_c &= N_p \cdot \frac{\sigma \langle v_{rel}\rangle \Delta t}{V_c} \cdot \frac{\tau}{\Delta t} \cdot \frac{2}{N} \\ &= 2 \cdot \frac{N_p}{N} \cdot \frac{\sigma \langle v_{rel}\rangle}{V_c} \cdot \tau \ . \end{aligned} \tag{3.26}$$

By substituting $\tau = \Gamma_{coll}^{-1} = 1/\langle n\rangle \sigma \langle v_{rel}\rangle$, the equation is further reduced to

$$\begin{aligned} N_c &= 2 \cdot \frac{N_p}{N} \cdot \frac{1}{\langle n\rangle V_c} \\ &\approx \frac{2}{\langle n\rangle V_c} \qquad \text{for large choices of } V_c. \end{aligned} \tag{3.27}$$

This is exactly the behavior seen in figure 3.4[4]. Choices of V_c such that $\langle n\rangle V_c \ll 2$ should therefore lead to accurate results. The recommendation of Ref. [45] to keep $\langle n\rangle V_c$ of the order of $10^{-3} - 10^{-2}$ is therefore extremely conservative. The simulations presented here typically use $\langle n\rangle V_c = 10^{-1}$, which is still well within the range of validity, but leads to large savings in computing time.

[4]The curve in figure 3.4 differs significantly from figure A.2 of Ref. [45], even though identical parameters were used. Since the results here are in perfect agreement with expectations, I assume that there must be a mistake in the documentation of Ref. [45].

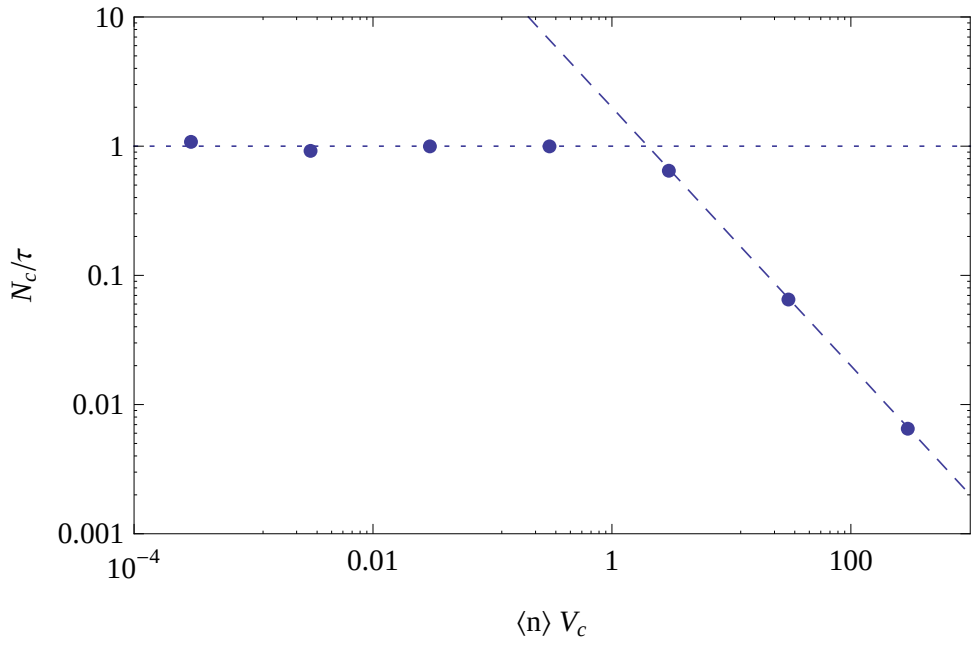

Figure 3.4: Effect of poor choice of search volume V_c on the Monte-Carlo simulation. The graph shows the number of collisions N_c per calculated collision time τ as a function of increasing V_c for a single-species gas in equilibrium. The dotted line marks $N_c/\tau = 1$, the dashed line shows the behavior when V_c is chosen to be too large, corresponding to $N_c \approx 2/\langle n \rangle V_c$. All simulations used 10^3 particles with $\langle p_{coll} \rangle = 10^{-2}$.

Particle numbers

There is one other input parameter which needs consideration. This parameter will not influence the results of the simulation but rather its practicality. Monte Carlo simulations require a considerable amount of computing resources. The computation time, which is dominated by the pairwise search for collision partners, scales roughly as the product of N_1, N_2, and the number of time steps, so simulations become impractical for $N \geq 10^5$. As an example, a simulation of 1.25×10^4 fermions of each species with 5000 time steps took approximately 8 hours an a computer with a 1.66 GHz processor and 2 gigabytes of RAM.

3.5 Results for β

In this section I will list predicted values of β for different Fermi-Fermi mixtures. One should note that in mixtures with equal particle numbers, the approximations made in equations 3.11 and 3.12 to determine these values for β lead to a slight overestimation (underestimation) of β for light (heavy) fermions, corresponding to values of η that are considerably smaller or larger than 1/2. Even though Eq. 3.19 allows β to be calculated directly (which is why no uncertainties are given here), this indicates that our prediction of β is more precise the smaller the mass difference between the fermions in the mixture.

Comparison of results from Monte Carlo simulations for various mass ratios with the theory curve in figure 3.1 suggests that the approximations hold well for mixtures with mass ratios up to $m_1/m_2 \approx 7$. This corresponds to limits of $\eta_1 = 0.875$ and $\eta_2 = 0.125$ in mixtures with equal particle numbers. The fermions in our experiment, ^{40}K and ^{6}Li have a mass ratio of $m_K/m_{Li} \approx 6.67$ that lies barely within these limits.

More accurate results for β in mixtures with large mass ratios can be obtained for the case where the particle number of the lighter species is larger than that of the heavy species, and the relaxations of both species take place on a similar timescale.

For mixtures of different spin states of a single species ($\eta = 1/2$), the expected value of β is 3. So far, only one mixture of two different fermionic species has been realized experimentally: ^{6}Li and ^{40}K, achieved both in our own lab [21], in Innsbruck and in Amsterdam [36]. However, several other alkali and alkaline earth metals have been trapped in magneto-optical traps or optical dipole traps ([29, 30, 31, 32, 33, 34]).

The following table lists values of β for different mixtures of these species. Only mixtures where the masses of the atoms yield values of η that lie within the range 0.125–0.875 are considered. The values of β in each row correspond to collisions of the element in the left column with the elements in the top row, e.g. the value 7.3 in the second row denotes the value of β for ^{40}K in collisions with ^{6}Li.

	^{6}Li	^{40}K	^{53}Cr	^{87}Sr	^{171}Yb	^{173}Yb	^{199}Hg	^{201}Hg
^{6}Li	3	2.0						
^{40}K	7.3	3	2.8	2.5	2.2	2.2		
^{53}Cr		3.3	3	2.7	2.3	2.3	2.2	2.2
^{87}Sr		3.9	3.5	3	2.6	2.5	2.5	2.5
^{171}Yb		5.5	4.7	3.8	3	3.0	2.9	2.9
^{173}Yb		5.6	4.8	3.8	3.0	3	2.9	2.9
^{199}Hg			5.1	4.0	3.1	3.1	3	3.0
^{201}Hg			5.2	4.0	3.1	3.1	3.0	3

Chapter 4

Experimental realization of cross-dimensional relaxation

This chapter gives an account of our experimental endeavors to observe cross-dimensional relaxation in a Fermi-Fermi mixture of ^{6}Li and ^{40}K.

An overview of the experimental setup is given in section 4.1. In the following I will outline the basic procedure of the measurements we have tried (section 4.2) and present an extensive discussion of the potential pitfalls and experimental constraints of a CDR measurement (section 4.3). The efforts we have made and the parameters we have used are described (section 4.4). Possible reasons for the negative outcome of our experiments are discussed and some suggestions for modified measurement techniques for possible further investigation in the future are presented in section 4.5.

4.1 Experimental setup

Our experiment is a platform for the generation of an ultracold Fermi-Fermi-Bose mixture of ^{6}Li, ^{40}K, and ^{87}Rb atoms. It is set up on two tables. On the first table, three laser systems, one for each species, provide the light required in the different phases of the experiment. A brief description of these systems is given in subsection 4.1.1. This laser light is transferred via optical fibers to the second table where the vacuum system is set up, the atoms are trapped, and the experiments are performed. The experimental apparatus is described in subsection 4.1.2. No contributions to the experimental setup were made for this thesis, so the outlines given here will be kept short, and the reader will be referred to the literature for further information, first and foremost to Matthias Taglieber's PhD thesis [22], in the course of which our experimental platform was developed from scratch.

4.1.1 Laser systems

Laser light with frequencies close to the relevant atomic resonances is needed for slowing, magneto-optical trapping and further cooling of the atoms; for optical pumping of the

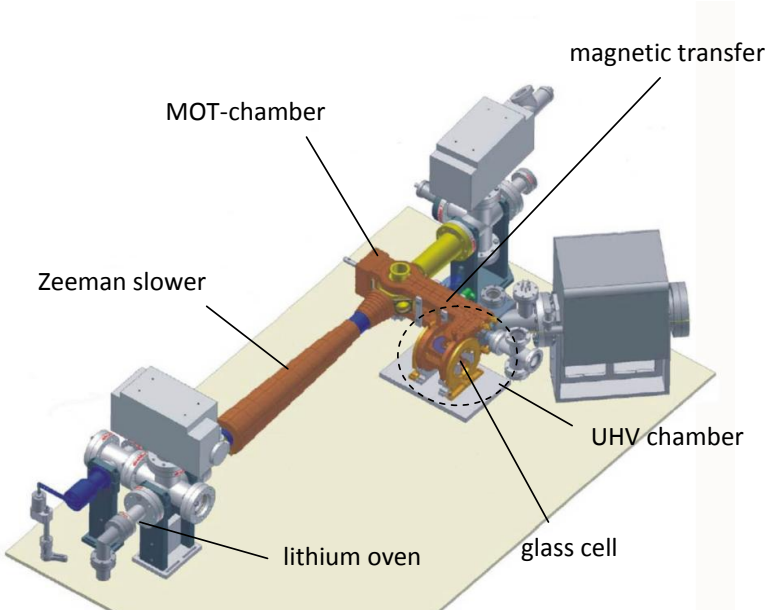

Figure 4.1: 3D-CAD drawing of the experimental apparatus.

atoms into their magnetically trappable states; and the final detection of the atoms using absorption imaging. An overview of the atomic energy levels relevant for the experiment and of the optical transitions driven during the experimental cycle is given in Ref. [22]. Details and schematic block diagrams of our laser systems can also be found there, while the setups of the lithium and potassium systems have been covered in detail in the diploma theses of Arne-Christian Voigt [74] and Florian Henkel [75], respectively; hence only some general information will be provided here.

The laser systems employed in our lab are completely diode-based. In the rubidium and the potassium systems a power boost is attained by the use of two tapered amplifier systems. Single-mode operation of the laser diodes is ensured either by means of either grating stabilization or injection locking, while long-term frequency stability is achieved by referencing to atomic transitions. Frequency shifts are realized by acousto-optical modulators (AOMs) in different configurations, i.e. single-, double- and quadruple-pass configuration, and the use of electro-optical modulators (EOMs) allows the laser power to be attenuated in a controlled way.

4.1.2 Experimental apparatus

The experimental setup is shown in Fig. 4.1. In order to reach the requisite low temperatures the atoms are first captured and pre-cooled in a three-species magneto-optical trap [21] at the center of a common magnetic quadrupole field in an initial vacuum chamber, which we will refer to as the "MOT chamber". Potassium and rubidium are loaded from background vapor produced by atomic vapor dispensers. However, the comparatively low saturation pressure of lithium requires higher temperatures during its sublimation to pro-

duce enough atoms to work with, which makes its vapor loading inefficient since only a small fraction of atoms have speeds below the typical MOT capture velocity. The lithium is therefore loaded into the MOT from a Zeeman-slowed atomic beam. The three clouds are then transferred into a magnetic quadrupole trap, also located in the MOT chamber. The lifetime of the clouds in this trap is limited by collisions of the trapped atoms with hot atoms from the residual background gas, so in order to achieve longer lifetimes the clouds are subsequently transferred into a second chamber consisting of an ultra high vacuum (UHV) glass cell with a residual pressure below 10^{-11} mbar. This transport is realized by driving a sequence of shifted quadrupole coils (so-called "transfer coils" [76]). At the end of the transport sequence the quadrupole trap is transformed into a quadrupole Ioffe-configuration trap (QUIC trap) to avoid losses due to Majorana spin flips at low temperatures[1]. In this final magnetic trap sympathetic cooling of the fermionic species with evaporatively cooled rubidium atoms produces an ultracold mixture of the three species with temperatures that can be low enough to reach quantum degeneracy [22, 78]. The atoms are then loaded from the QUIC trap into an optical dipole trap (ODT) produced by a pair of perpendicular laser beams with foci coinciding at the center of the magnetic trap.

The ODT can be realized in either of two configurations, corresponding to combinations of the vertical trap beam aligned along the z-axis, referred to as ODT2, with either of the horizontal beams, referred to as ODT1 (along x) and ODT3 (along y), respectively. The $1/e^2$ radii of the beams at the trap center are $w_{ODT1} = 52$ μm, $w_{ODT2} = 44$ μm, and $w_{ODT3} = 43$ μm. The horizontal and vertical beams have perpendicular polarizations and a frequency difference of 220 MHz, which is achieved by the use of two AOMs in the ODT setup[2]. However, there is no frequency shift between the two horizontal beams, and so even small deviations from perfectly perpendicular polarizations could result in optical lattice effects. This is why no configuration including the two horizontal or all three beams is used.

As indicated in Fig. 4.2, atoms trapped in the ODT12 configuration are imaged along the direction of the ODT3 beam, which is perpendicular to the symmetry axis of the QUIC trap (side-transverse imaging[3]). In the ODT23 configuration the atoms are detected by imaging along the axis of the ODT1 beam, coaxial with the symmetry axis of the QUIC trap (side-axial imaging; cf. Fig. 4.2).

4.2 Procedure

In all of the experiments described below, clouds of ^{6}Li, ^{40}K, and ^{87}Rb atoms are first captured and pre-cooled in the MOT as described in [21]. During the cooling process, the three species are optically pumped into their most strongly confined and collisionally stable

[1] Details of the transfer coils and the QUIC trap in our experiments can be found in Christoph Eigenwillig's diploma thesis [77]

[2] details of this setup can be found in Wolfgang Wieser's diploma thesis [70]

[3] For details of the imaging see [22]

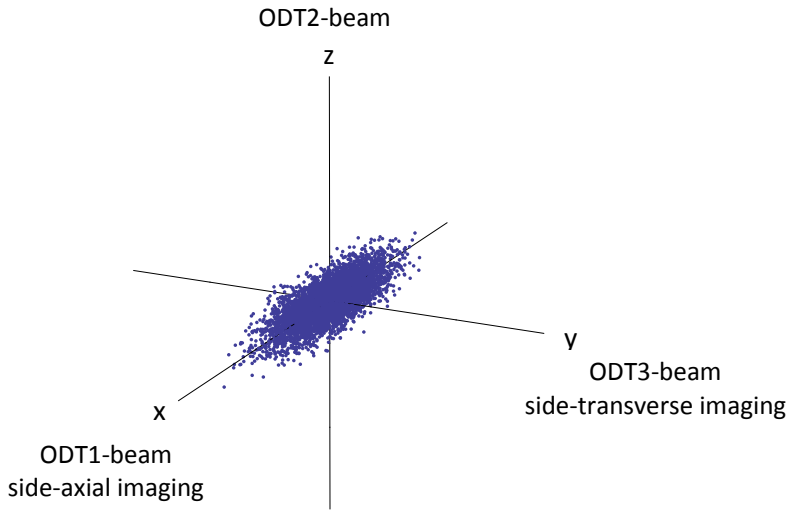

Figure 4.2: The atomic cloud in the QUIC-trap forms a cigar-shaped distribution aligned along the x-axis. We call the imaging along the y-axis 'side transverse', and that along the x-axis 'side axial'.

states ^{87}Rb $|F = 2, m_F = 2\rangle$, ^{40}K $|9/2, 9/2\rangle$, and ^{6}Li $|3/2, 3/2\rangle$, before being transferred into the QUIC trap, where the sympathetic cooling of lithium and potassium with the evaporatively cooled rubidium takes place [78]. After ^{6}Li and ^{40}K have been cooled to the desired temperatures (see below), rubidium is evaporated through the trap bottom, and any residual ^{87}Rb atoms in the $|F = 2\rangle$ manifold are removed by a resonant light pulse. Thereafter the Fermi-Fermi mixture is adiabatically transferred into the ODT, where first lithium and then potassium are transferred into the absolute ground states ^{6}Li $|1/2, 1/2\rangle$ and ^{40}K $|9/2, -9/2\rangle$ by an adiabatic rapid passage (ARP) at 20.6 G. This order is advantageous because, as a consequence of the inverted hyperfine structure of ^{40}K, it suppresses losses due to interspecies spin relaxations. Transfer efficiencies of the ARPs are almost complete for both species, and the non-transferred fractions are below the detection threshold [23].

The basic idea of what we have tried is as follows: In order to prepare the system for the measurements, the atoms are loaded into the ODT and held for a sufficiently long time to allow both species to reach thermal equilibrium before an energy anisotropy is introduced between different spatial dimensions. This anisotropy is created by ramping the power in one of the ODT beams either down or up, leading to an adiabatic change of the trapping frequencies and thus producing an energy anisotropy between different directions, as the change in energy in a given direction is proportional to that of the trapping frequencies. Note that in this case of an ODT formed by a pair of crossed beams, the trapping frequency along the direction of the beam which is ramped down stays almost the same, whereas the trapping frequencies in the directions perpendicular to the beam axis change by different amounts. To understand why, consider the trapping potential of each of the two beams

individually. As shown in chapter 2, a Gaussian beam has a small intensity gradient and therefore only weak confinement along its propagation axis. Perpendicular to this axis, the intensity gradient – and thus the confinement – is large. In a crossed ODT consisting of beams along the y- and z-directions, the confinement and therefore the trapping frequencies are largest in the x direction, which is perpendicular to the propagation axes of both beams. If now the beam along z is now ramped down, the trapping frequency in the x direction is somewhat compensated by the strong confinement due to the other beam propagating along y. The trapping frequency in the y direction, however, will change dramatically since this is the axis of weaker confinement of the other beam.

Once the energy anisotropy has been introduced into the system, the trap beams are kept steady, and the rethermalization process is observed. The time constant of the cross-dimensional relaxation is extracted by holding the mixture for variable times in the final trap and then measuring the aspect ratios of the clouds after time-of-flight expansion. It was shown in chapter 2 that the square of the aspect ratio is proportional to the ratio of energies in the the respective directions. In addition, the aspect ratio is hardly sensitive to shot-to-shot variations in the absolute temperature of the cloud before the energy anisotropy is created. From the absorption images after every shot one also determines particle numbers of both species.

4.3 Experimental constraints

When trying to observe cross-dimensional relaxation, several constraints must be kept in mind. Firstly, it is crucial to work at high enough temperatures to avoid Pauli blocking, so the relaxation is not artificially slowed down. In agreement with [79], we therefore used temperatures in the range of $T/T_F = 1 - 1.5$. For an easier theoretical description of the relaxation process, it is also important that the atoms remain in the harmonic region of the trap. The size of this region is dependent on the light intensity in the trapping beams and is smaller for low intensities. The distribution of the atoms in the trap, however, is determined by the temperature, leading to a maximum temperature dependent on the trapping potential, that should not be exceeded.

Secondly, it is important to work at densities and scattering lengths which are low enough to ensure that the experiment is performed in the collisionless regime, but which at the same time give rise to suitable mean times between collisions. Here 'suitable' means long enough to be resolved experimentally, (i.e. ideally of the order of 10 ms), but not too long, since at holding times of the order of 100 ms atom loss from the trap becomes problematic for experimentally available ODT powers.

As a side note: So far, the constraints suggest that one could also use our magnetic trap for the CDR measurements. Due to the much lower trapping frequencies, however, the mean times between collisions are two orders of magnitude longer than in the ODT at the required temperatures and densities.

From the theoretical model in chapter 3 we know that in the mixture of ^{6}Li and ^{40}K the lithium atoms need an average of two (2.0) collisions for equilibration, whereas it is

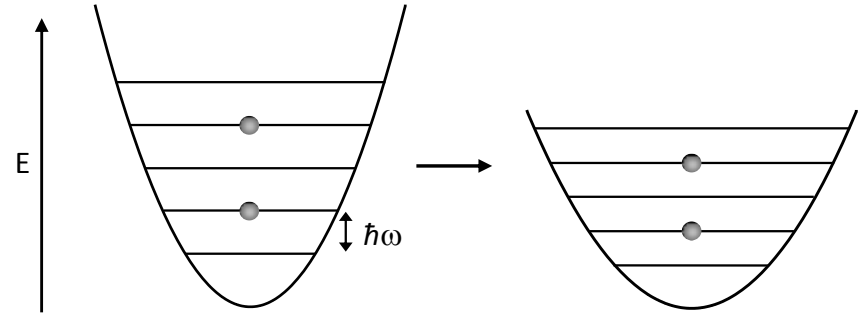

Figure 4.3: Adiabatic change of the trapping frequencies. Particles remain in the same energy eigenstate.

more than seven (7.3) collisions for potassium. The relaxation of both species on a similar time scale can therefore be achieved with a mixture where the particle numbers of lithium in the trap are a factor of 3–4 times higher than those of potassium. Whatever the particle numbers of both species, it is essential that their ratio remains stable from shot to shot in order to obtain data suitable for analysis. For the same reason it is crucial to have well-defined anisotropies. It is therefore necessary to wait until the gas in the trap is fully thermalized before the ramp inroducing the anisotropy takes place.

The ramping of the beam has to be performed slowly enough for the trapping frequencies to change adiabatically – adiabaticity is given for $\partial_t \omega \ll \omega^2$ – so that no phase space density is lost or oscillation is stimulated. Also, if the change is not adiabatic, the gas will no more be thermalized in each directions, i.e. not have a Gaussian energy distribution in the respective spatial dimensions. The ramp, however, has to be done on a time scale much shorter than the mean time between collisions in the gas to avoid rethermalization during the ramp so that the relaxation already during the ramp is negligible and the signal stays strong. Figure 4.3 illustrates the adiabatic change of the trapping potential and its effect on particles in energy eigenstates $\varepsilon_n = n\hbar\omega$.

The mean time between collisions, defined above as $\tau = \Gamma_{coll}^{-1} = (\langle n \rangle \, \sigma \, \langle v_{rel} \rangle)^{-1}$, is temperature dependent and shorter at higher energies[4] since with increasing temperature $\langle n \rangle$ decreases more slowly than $\langle v_{rel} \rangle$ increases. Starting at higher temperatures therefore reduces the holding time required for equilibration before the actual part of the measurement begins, which is why in most measurements we chose to ramp the beam down. Due to their mass difference lithium and potassium have a different graviational sag in the trap that leads to a decrease in the density overlap and thus to an increase of the mean time between collisions when the trapping frequency in the vertical direction is lowered. To avoid this effect, only the vertical beam is used for the creation of energy anisotropies, as a change in its intensity mainly affects the trapping frequencies in the horizontal plane.

When the vertical (z) beam is ramped down (up), the trapping frequencies in the x and y directions hange to lower (higher) values, leading to a decrease (increase) in

[4]Note that for our estimates of τ, we used $\sigma = (70a_0)^2$, which is suggested by (ref!). Here, a_0 is the Bohr radius.

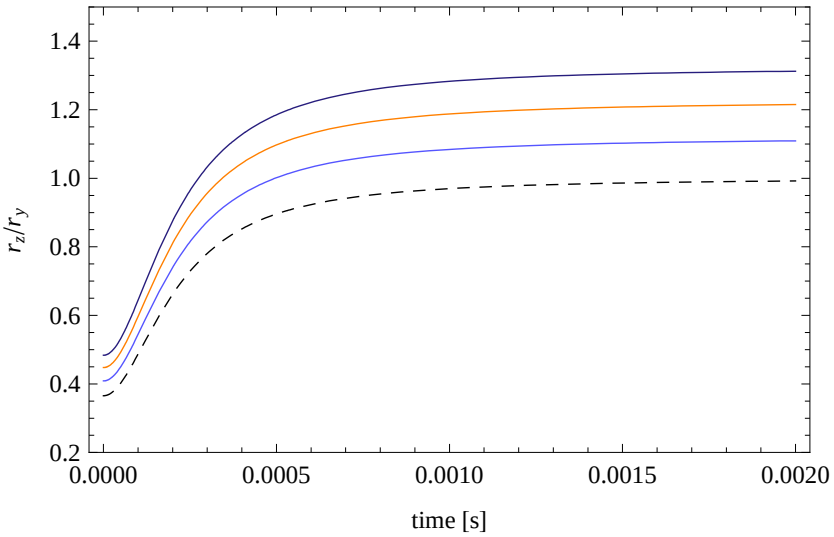

Figure 4.4: Expected aspect ratio for different energy anisotropies: Plotted is the calculated aspect ratio r_z/r_y of the lithium cloud as a function of the time of flight for trapping frequencies $(\nu_x, \nu_y, \nu_z) = (1707, 586, 1603)$ Hz. The dashed line depicts the aspect ratio of a thermalized cloud, the colored lines show the ratio for different energy anisotropies during the rethermalization process: $E_z/E_y = 1.73$ (blue), $E_z/E_y = 1.5$ (orange), $E_z/E_y = 1.25$ (light blue).

temperature in the respective directions. The energy change in a given direction after the ramp is then proportional to the change of the corresponding trapping frequency $E_{new,i} = E_{initial} \cdot \omega_{new,i}/\omega_{initial,i}$ with $i = x, y, z$.

The anisotropies in the gas can then be determined by calculating the energy ratios after the ramp with respect to the lowest of the three energies. It is important to note that in the experiment the aspect ratio of the cloud is measured, which is not proportional to the energy ratio, but only to its square root $\sqrt{E_i/E_j}$. For anisotropies $\Omega \leq 1.7$ qualified as "reasonable" in the previous chapter, one therefore expects a signal of ~ 1.3 times the aspect ratio relaxing towards 1 times the aspect ratio. Clearly, this is not a very strong signal, so a good signal-to-noise ratio is required in order to obtain useful data. Figure 4.4 gives an impression of the sort of signal we were hoping to detect. The aspect ratio is determined from absorption images after time-of-flight expansion. This is another reason why the trapping potential is required to be as close to harmonic as possible since if it is not, the ballistic expansion of the cloud does not follow the description given in subsection 2.1.2.

One factor that would clearly influence the relaxation process is collisions of the lithium and potassium atoms with either rubidium atoms or different spin-states of the same species left in the trap. The number of residual rubidium atoms and the fraction of different spin-states of lithium and potassium left in the trap after the state-preparation were below the detection threshold, so that we can savely neglect their effect on the relaxation. While rubidium can only be checked for by taking an absorption image, there are two ways to verify

Figure 4.5: Illustrative example of wings as seen in the side-transverse imaging. The figure shows an intra-trap image of potassium taken after 100 ms of holding following a 125 ms ramp of the ODT. The beam powers were ODT1 = 2.2 W, ODT2 = 1.1 W corresponding to trapping frequencies $\nu_x = 730$ Hz, $\nu_y = 1034$ Hz, and $\nu_z = 732$ Hz. The circular cloud at the trap center has a diameter of about 22 μm.

the absence of spin-mixtures after the state-preparation. One is a Stern-Gerlach separation of the different spin-states, and the second is to prepare a cloud of only one species, either lithium or potassium, in the trap and create an energy anisotropy. Since s-wave collisions are suppressed for identical fermions, no rethermalization should be observed.

4.4 Measurements

On starting the experiment, it soon became clear that we would not be able to use the ODT12 configuration for our measurements. Although we tried a number of different loading schemes from the QUIC trap into the ODT (linear and nonlinear QUIC ramps with durations of 100 to 500 ms, ODT ramps ranging from 10 to 125 ms), we found no way to avoid 'wings' – i.e. atoms trapped along the ODT1 beam outside the harmonic region at the trap center (cf. Fig. 4.5). These wings are a consequence of the loading from the QUIC trap, whose axis coincides with that of the ODT1 beam. The approximate distribution of the atoms in the QUIC trap and the axes of the ODT beams are shown in Fig. 4.2. At the low temperatures normally used in our experiments with quantum-degenerate gases, these wings never were a problem since the cloud in the trap center was spatially distinct from the wings. At the comparatively high temperatures required for the CDR measurement, however, the cloud in the center is more expanded, and even if the wings contain only a small fraction of the total atoms, in which case their effect on the relaxation may be neglected, fitting of the cloud sizes is not accurate enough with wings present as the signal is small anyway.

In the ODT23 trap configuration, where both trapping beams are in a plane perpendicular to the axis of the QUIC trap, no wings appeared in the absorption images. A clear disadvantage of this configuration, however, is that the ODT3 beam does not have independent intensity stabilization, but is stabilized via the ODT1 beam. A clear disadvantage of this configuration is, however, that the ODT3 beam does not have an intensity stabilization on its own but is stabilized via the ODT1 beam. In the current setup, the two horizontal beams are split only after a common AOM by the usual means of a half-wave plate followed by a polarizing beamsplitter. In principle, this allows for arbitrary power

ratios of the two beams; in order to have the ODT3 beam properly stabilized, however, it is advisable not to choose a too low intensity for the ODT1 beam, which limits the power available in the experiment as compared with the ODT12 configuration. The maximum intensity ratio used in our measurements was ODT3 : ODT1 = 2 : 1.

In the measurements described below, the QUIC trap was switched off within 100 ms and the atoms were held in the ODT for a further 50 ms for thermalization and state preparation purposes before an energy anisotropy was introduced. This anisotropy was created by ramping the power of the vertical trap beam (ODT2) while the power of the horizontal beam was kept constant. Typical ramp durations were 8 - 10 ms, which is in accordance with the considerations outlined above. In most cases, the ODT2 beam was ramped down and not up, since this way less time is required for the initial equilibration before the energy anisotropy is introduced.

In the following an examples is presented to illustrate the difficulties we have had. The parameters used in the other runs were similar to those used here. In this exemplary run the power of the horizontal beam was set to 1.6 W, and the power of the vertical beam was ramped from 0.85 W down to 0.30 W within 8 ms. The resulting intial anisotropies were $E_z/E_y = 1.73$ and $E_x/E_y = 1.55$, the former of which would be observed. These anisotropies are slightly higher than recommended above but in order to obtain first signals of CDR at all, they are a valid choice since we can only detect the square root of the anisotropy, $\sqrt{E_z/E_y} = 1.32$, which is a small signal. Figure 4.4 shows the expected aspect radio of the expanding cloud as a function of the time of flight for different stages of the relaxation process. The particle numbers in this run were $N_K = 5 \times 10^4$ $N_{Li} = 7 \times 10^4$, so for a temperature $T/T_F \sim 1.5$, the average densities before (after) the ramp were $\langle n_{Li} \rangle_K = 2.2 \times 10^{12}$ cm^{-3} (1.5×10^{12} cm^{-3}) and $\langle n_K \rangle_{Li} = 1.6 \times 10^{12}$ cm^{-3} (1.1×10^{12} cm^{-3}). The respective mean times between collision were $\tau_K = 15$ ms (24 ms) and $\tau_{Li} = 21$ ms (35 ms). Knowing that lithium would on average need two collisions per particle for rethermalization, we expected to observe a clear signal within the first 100 ms after ramping. In order to get a reliable fit of the aspect ratio, the time of flight for lithium was chosen such that the ratio was stable against slight variations in the expansion time. Figure 4.4 shows that immediately after the release of the cloud from the trap the density distrubtion and therefore the ratio undergoes rapid change that is dependent on the trapping frequencies whereas the long term evolution dependends only on the energies of the cloud in the respective directions. A viable choice was therefore a time of flight of 2 ms for lithium. Due to technical limitations, the potassium cloud could be imaged only 3 ms later, where the low optical density did not permit the aspect ratio to be fitted properly. While we could very clearly detect the initial anisotropy, we were not able to observe a relaxation or any defined behavior at all after various holding times except for large fluctuations. What we did observe, however, were particle losses which made accurate fitting after a holding time of 100 ms impossible. The ratio of trap depth over temperature was around 21 for lithium and almost twice as much for potassium, so the losses in lithium were more severe. In other runs with slightly altered parameters our observations were similar, in one case even suggesting a small cooling effect on potassium by the lithium atoms lost from the trap. In an attempt ro ramp the power of the vertical beam up (1.5 W in the horizontal beam,

vertical beam 0.55 W up to 1.2 W within 9 ms) to create a higher trap depth for lithium, we were also able to observe the initial anisotropy but could not observe any relaxation due to a bad signal-to-noise ratio and fluctuations in the particle numbers.

4.5 Discussion and outlook

As simple as the basic principle of the measurements described in this chapter may seem, as challenging is its realization.

Facing major constraints regarding the possible holding times in the trap and the quality of the signal needed, a right set of parameters have to be found in order to obtain analyzable data. As we have not been able to obtain usable results by the time this thesis goes to print, more time will have to be invested.

A good signal requires large anisotropies and those can only be achieved by adiabatically changing the power of one of the beams by a considerable amount. As a consequence, the mean time between collisions is comparatively long ($\sim$ 30 ms, of course dependent on the exact parameters) either during the intial thermalization after loading from the QUIC trap into the ODT (if the power is ramped up) or during the CDR process after the ramp (if the power is ramped down). Therefore, very long holding times are required in total, and this leads to a loss of atoms from the trap.

One way to resolve this problem might be the use of higher intensities in the trapping beams, which would lead to a stronger confinement and higher collisions rates and thus shorter time scales of the relaxation process.

There is also another method to create a cross-dimensional energy anisotropy, which we have not yet tried. Intensity-modulation of a trap beam with a frequency that is close to the twice the trapping frequency $2\omega_i$ or one of the subharmonic frequencies $2\omega_i/n$ leads to an exponential increase in the mean energy of the respective direction i. This is called parametric heating [80]. Compared with our procedure of simply ramping one of the beams down or up, it is more complicated to calculate the energy anisotropy in this case. It might, however, be an option worth trying since large anisotropies can be created while the mean beam power is kept high.

In general, the method to use CDR in order to determine the elastic scattering cross-section has limited accuracy because of systematic uncertainties in the atom number, which is typically determined from absorption imaging. Experimental imperfections such as frequency jitter, imperfect polarization of the probe beam, or fluctuation and tilt of the magnetic field during imaging tend to reduce the absorption of the probe beam, which leads to an underestimation of the particle number. Cross-dimensional relaxation processes in lithium and potassium are very sensitive to variations in the particle number, and for the fitting model which determines the elastic scattering cross-section, knowledge of the particle numbers of both species is crucial.

In the measurements presented here, the magnetic field that ensured spin-polarization in the mixture was chosen to be 20 G. At a magnetic field of this strength, the elastic scattering cross-section between lithium and potassium can be considered independent of

the magnetic field. Once the problems described above have been resolved, it will be interesting to probe the scattering cross-section at fields close to a Feshbach resonance, where two colliding atoms couple resonantly to a bound molecular state and the scattering cross-section tends to unitarity [36].

Chapter 5

Conclusion

In this thesis, a kinetic model for cross-dimensional rethermalization in Fermi-Fermi mixtures was developed that allows for accurate predictions of the number β of collisions per fermion needed for equilibration as a function of the masses of the fermions in the mixture. Detailed classical Monte Carlo simulations were carried out to test the validity of these predictions for a wide range of parameters. Effects due to the finite initial departure from thermal equilibrium were addressed, and limits on the magnitudes of the initial anisotropies were derived. It was shown that the difference in mass between the fermions in the mixture can lead to a factor of ~ 4 difference in the values of β for light and heavy fermions. For the mixture of ^{6}Li and ^{40}K used in our experiment the respective values were determined to be $\beta_{Li} = 2.0$ and $\beta_K = 7.3$.

Based on these theoretical predictions, attempts were made to probe the elastic collision cross section and thus the absolute value of the s-wave scattering length of the ultracold, dilute, nondegenerate mixture of ^{6}Li and ^{40}K.

Once the experimental difficulties that hampered these attempts have been resolved, rethermalization measurements of this type can be used not only to determine the elastic collision cross section at a magnetic field of zero magnetic field, i.e. at a magnetic guidance field that has no influence on the scattering length, but also to map out Feshbach resonances.

Appendix A

Thermal averages with different energy anisotropies for each species

Although we assume the energy anisotropy to be the same for each species at the beginning and the end of the relaxation, i.e. Ω_x, Ω_y and 1, respectively, the fact that β_1 and β_2 are generally different for two species with unequal masses $m_1 \neq m_2$ means that the two species will have different anisotropies at intermediate times.

The theory presented in section 3.2 assumes separable Gaussian distributions for each species in each direction. When calculating thermal averages, however, it is important to note that the center-of-mass (c.m.) and relative velocities are generally correlated if the energy anisotropy is not the same for each species:

$$\frac{1}{2}\left(\frac{m_1 v_{1,i}^2}{E_{1,i}} + \frac{m_2 v_{2,i}^2}{E_{2,i}}\right) = \left(\frac{M V_{c.m.,i}^2}{\varepsilon_{c.m.,i}} + \frac{\mu v_{rel,i}}{\varepsilon_{rel,i}}\right) - \mu \delta_i V_{c.m.,i} v_{rel,i} \tag{A.1}$$

Here $E_{\sigma,i}$ is the mean energy for species σ in the i^{th} direction, and we have defined[1]:

$$\begin{aligned} \varepsilon_{c.m.,i} &= \frac{(m_1+m_2)\, E_{1,i} E_{2,i}}{m_2 E_{1,i} + m_1 E_{2,i}} \\ \varepsilon_{rel,i} &= \frac{(m_1+m_2)\, E_{1,i} E_{2,i}}{m_1 E_{1,i} + m_2 E_{2,i}} \\ \delta_i &= \frac{E_{1,i} - E_{2,i}}{E_{1,i} E_{2,i}}. \end{aligned} \tag{A.2}$$

To obtain the approximations made in equations 3.11 and 3.12, we are interested in ratios of the type

$$\frac{\left\langle v_{rel} v_{rel,i}^2 \right\rangle}{\left\langle v_{rel} \right\rangle \left\langle v_{rel,i}^2 \right\rangle}, \tag{A.3}$$

[1]Note that our definition of $\varepsilon_{rel,i}$ differs from that given in Ref. [45]. The definition there is an error, all calculations used the correct form (private communication).

and

$$\frac{\langle v_{rel} V_{c.m.,i} v_{rel,i} \rangle}{\langle v_{rel} \rangle \langle V_{c.m.,i} v_{rel,i} \rangle}, \tag{A.4}$$

which, in accordance with [71], we claim to be roughly equal to 4/3 for "reasonable" anisotropies Ω_x and Ω_y (see below). By using the distribution function $\exp \exp (-H/k_B T)$ along with the definitions above, one can calculate the following averages:

$$\begin{aligned} \langle v_{rel,i}^2 \rangle &= \frac{E_{1,i}}{m_1} + \frac{E_{2,i}}{m_2} \\ \langle V_{c.m.,i} v_{rel,i} \rangle &= \frac{E_{1,i} - E_{2,i}}{m_1 + m_2} \end{aligned} \tag{A.5}$$

For the other averages of interest

$$\begin{gathered} \langle v_{rel} \rangle, \\ \langle v_{rel} v_{rel,i}^2 \rangle, \\ \langle v_{rel} V_{c.m.,i} v_{rel,i} \rangle, \end{gathered}$$

one can also find analytic solutions if there is a cylindrical symmetry $\Omega_x = \Omega_y$ [45]. In the general case, where $\Omega_x \neq \Omega_y$, this appears not to be possible. In order to determine an upper limit on the size of a "reasonable" anisotropy, we therefore have to rely on numerical integration[2].

The limit on the magnitudes of the initial anisotropies were chosen so that the ratios in equations A.3 and A.4 deviate from 4/3 by a maximum of 5% during the relaxation process; i.e. the ratios stay between 1.40 and 1.27. For any choice of Ω_y, this allows an upper limit for Ω_x to be given:

Ω_y	Ω_x
1.1	< 1.5
$1.2 - 1.3$	< 1.6
$1.4 - 1.5$	< 1.7
$1.6 - 1.7$	< 1.8

Figures A.1 and A.2 show the ratios of equations A.3 and A.4 as a function of the mass ratio m_1/m_2 for varying anisotropies $\Omega_{x,1}$, $\Omega_{y,1}$, $\Omega_{x,2}$, and $\Omega_{y,1}$. Plot B in A.2 is included for the sake of completeness, although we strongly recommend using the axes with the larger anisotropy for fitting due to the better signal-to-noise ratio. Jittery lines in Fig. A.1 are the result of difficulties with the numerical integration. The integrals over the ratios given in equation A.3 can be reduced to a three-dimensional representation which Mathematica can handle well, whereas integrals of the type presented in equation A.1 require numerical integration in four dimensions, which for some parameters led to problems that couldn't be resolved in appropriate time.

[2] As a cross-check, the algorithm (Mathematica's Global Adaptive) was also used for calculations where comparison with analytic solutions was possible.

To give an impression of how the ratios of equation A.3 change during a realistic rethermalization process, Fig. A.3 plots the time evolution of $\langle v_{rel} v_{rel,x}^2 \rangle / \langle v_{rel} \rangle \langle v_{rel,x}^2 \rangle$ and $\langle v_{rel} v_{rel,z}^2 \rangle / \langle v_{rel} \rangle \langle v_{rel,z}^2 \rangle$ for a mixture of ^{6}Li and ^{40}K. The anisotropies $\Omega_{x,\sigma}(t)$ and $\Omega_{y,\sigma}(t)$ used to obtain these plots were taken from the relaxation curves of Fig. 3.2, where parameters were used that correspond to those of our experiment.

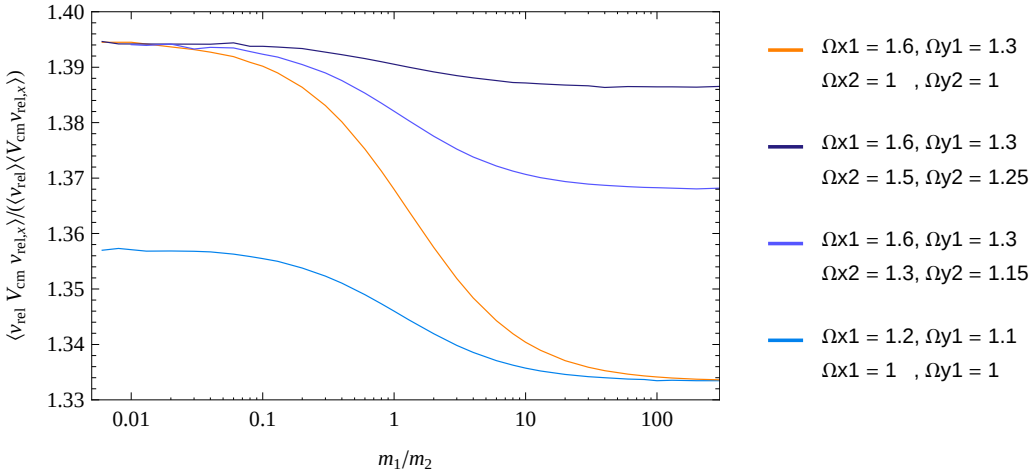

Figure A.1: The value of $\langle v_{rel} V_{c.m.,x} v_{rel,x} \rangle / \langle v_{rel} \rangle \langle V_{c.m.,x} v_{rel,x} \rangle$ for different anisotropies and mass ratios. The jittery parts result from problems with the numerical integration. Comparison with plot A in A.2 suggests that $\frac{\langle v_{rel} v_{rel,i}^2 \rangle}{\langle v_{rel} \rangle \langle v_{rel,i}^2 \rangle} \approx \frac{\langle v_{rel} V_{c.m.,i} v_{rel,i} \rangle}{\langle v_{rel} \rangle \langle V_{c.m.,i} v_{rel,i} \rangle}$, which can be shown to hold exactly in the cylindrically symmetric case[45].

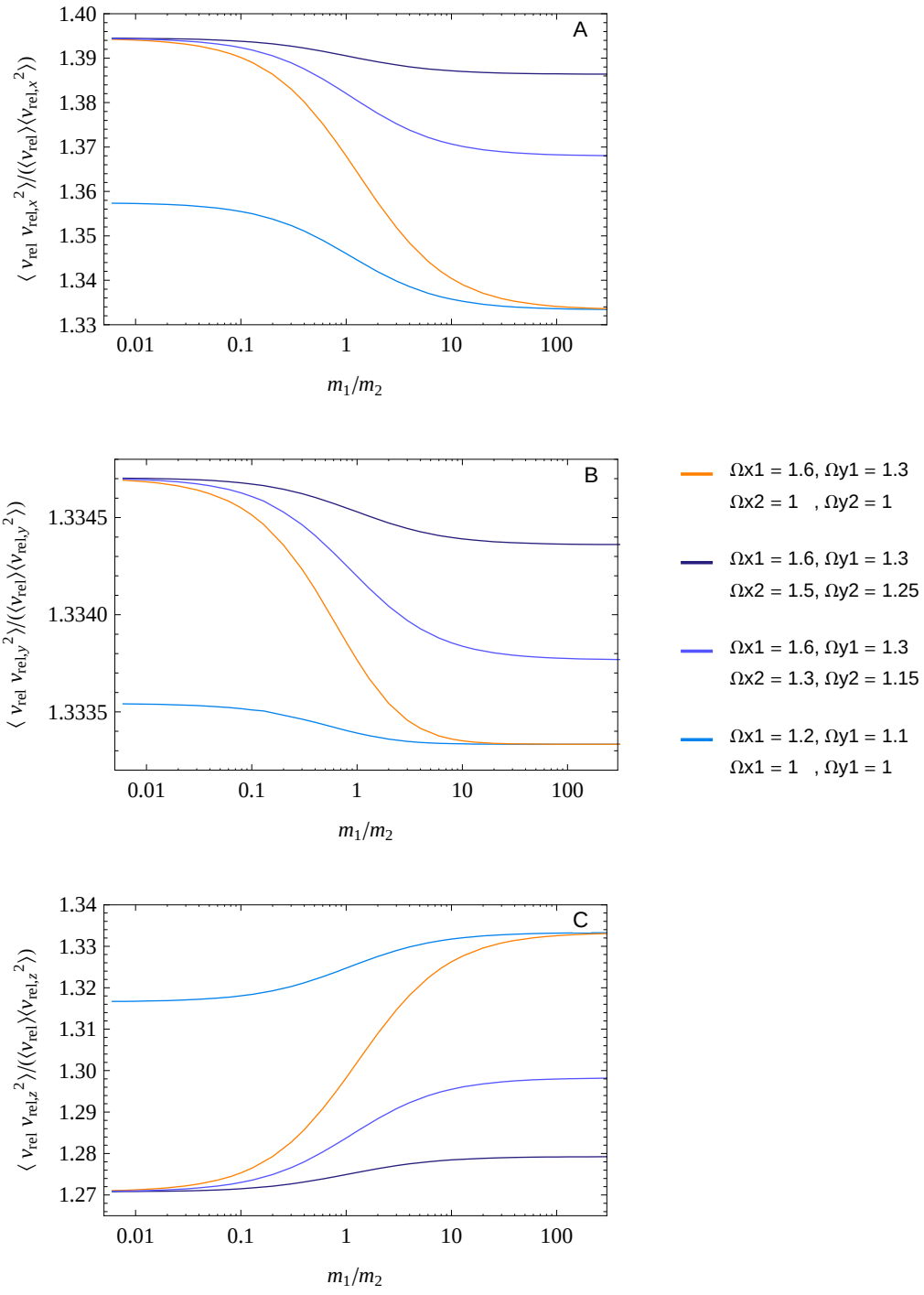

Figure A.2: The value of $\left\langle v_{rel} v_{rel,i}^2 \right\rangle / \langle v_{rel} \rangle \left\langle v_{rel,i}^2 \right\rangle$ for different anisotropies and mass ratios.

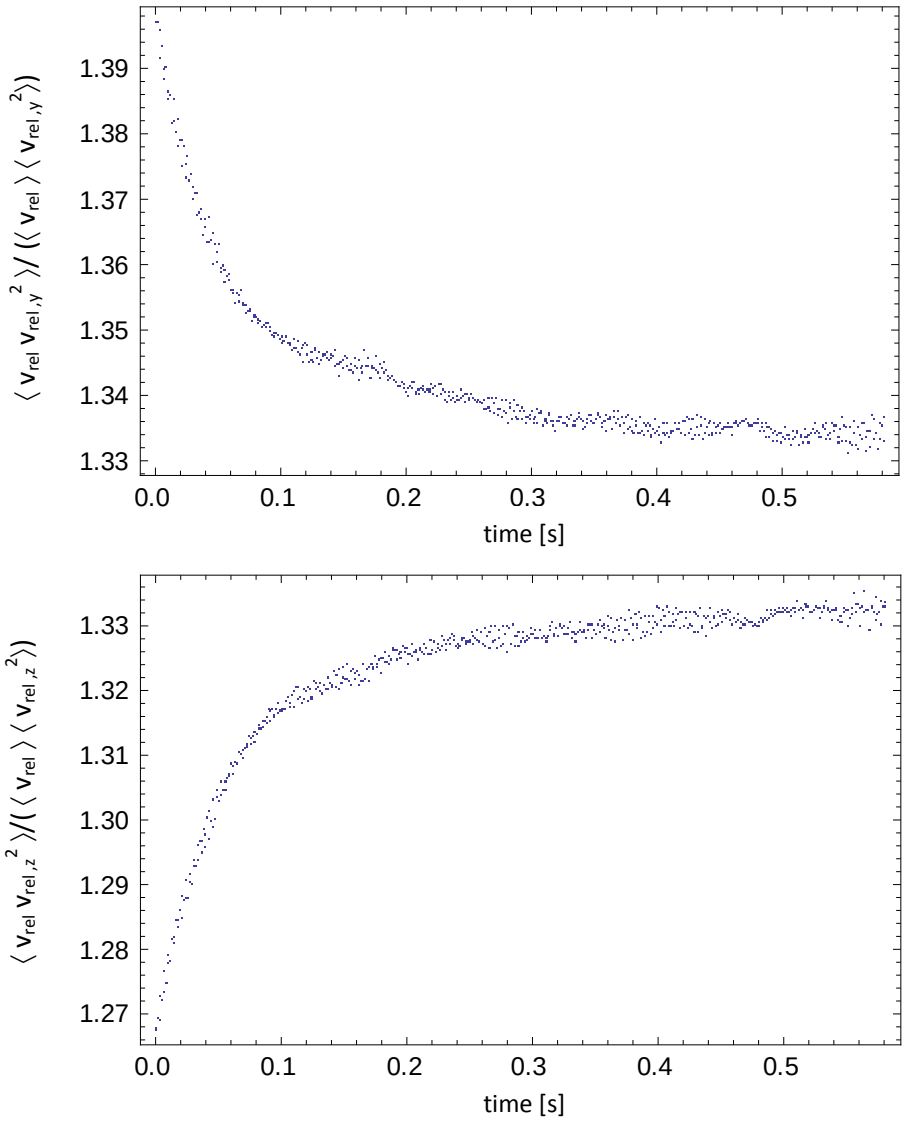

Figure A.3: Time evolution of the ratio $\left\langle v_{rel} v_{rel,i}^2 \right\rangle / \left\langle v_{rel} \right\rangle \left\langle v_{rel,i}^2 \right\rangle$ in the y and z directions corresponding to the relaxation curves of Fig. 3.2.

Bibliography

[1] S. N. Bose, "Plancks Gesetz und Lichtquantenhypothese," *Zeitschrift für Physik* **26** (1924) 178–181.

[2] A. Einstein, "Quantentheorie des einatomigen idealen Gases," *Sitzungsber. Kgl. Preuss. Akad. Wiss.* (1924) 261.

[3] A. Einstein, "Quantentheorie des einatomigen idealen Gases: Zweite Abhandlung," *Sitzungsber. Kgl. Preuss. Akad. Wiss.* (1925) 3–14.

[4] E. Fermi, "Zur Quantelung des idealen einatomigen Gases," *Zeitschrift für Physik* **36** (1926) 902–912.

[5] P. A. M. Dirac, "On the Theory of Quantum Mechanics," *Proceedings of the Royal Society* **A 112** (1926) 661–77.

[6] K. B. Davis, M. O. Mewes, M. R. Andrews, N. J. van Druten, D. S. Durfee, D. M. Kurn, and W. Ketterle, "Bose-Einstein Condensation in a Gas of Sodium Atoms," *Phys. Rev. Lett.* **75** (Nov, 1995) 3969–3973.

[7] M. H. Anderson, J. R. Ensher, M. R. Matthews, C. E. Wieman, and E. A. Cornell, "Observation of Bose-Einstein Condensation in a Dilute Atomic Vapor," *Science* **269** (1995), no. 5221, 198–201.

[8] B. DeMarco and D. S. Jin, "Onset of Fermi Degeneracy in a Trapped Atomic Gas," *Science* **285** (1999), no. 5434, 1703–1706.

[9] A. G. Truscott, K. E. Strecker, W. I. McAlexander, G. B. Partridge, and R. G. Hulet, "Observation of Fermi Pressure in a Gas of Trapped Atoms," *Science* **291** (2001), no. 5513, 2570–2572.

[10] F. Schreck, G. Ferrari, K. L. Corwin, J. Cubizolles, L. Khaykovich, M.-O. Mewes, and C. Salomon, "Sympathetic cooling of bosonic and fermionic lithium gases towards quantum degeneracy," *Phys. Rev. A* **64** (Jun, 2001) 011402.

[11] M. Greiner, C. A. Regal, and D. S. Jin, "Emergence of a molecular Bose-Einstein condensate from a Fermi gas," *Nature* **426** (2003) 537.

[12] S. Jochim, M. Bartenstein, A. Altmeyer, G. Hendl, S. Riedl, C. Chin, J. Hecker Denschlag, and R. Grimm, "Bose-Einstein Condensation of Molecules," *Science* **302** (2003), no. 5653, 2101–2103.

[13] M. W. Zwierlein, C. A. Stan, C. H. Schunck, S. M. F. Raupach, S. Gupta, Z. Hadzibabic, and W. Ketterle, "Observation of Bose-Einstein Condensation of Molecules," *Phys. Rev. Lett.* **91** (Dec, 2003) 250401.

[14] W. C. Stwalley, "Stability of Spin-Aligned Hydrogen at Low Temperatures and High Magnetic Fields: New Field-Dependent Scattering Resonances and Predissociations," *Phys. Rev. Lett.* **37** (1976), no. 24, 1628–1631.

[15] E. Tiesinga, B. J. Verhaar, and H. T. C. Stoof, "Threshold and resonance phenomena in ultracold ground-state collisions," *Phys. Rev. A* **47** (1993), no. 5, 4114–4122.

[16] S. Inouye, M. R. Andrews, J. Stenger, H.-J. Miesner, D. M. Stamper-Kurn, and W. Ketterle, "Observation of Feshbach resonances in a BoseÐEinstein condensate," *Nature* **392** (1998) 151.

[17] A. J. Leggett, *Modern Trends in the Theory of Condensed Matter*. Springer-Verlag, Berlin, 1980.

[18] H. T. C. Stoof, M. Houbiers, C. A. Sackett, and R. G. Hulet, "Superfluidity of Spin-Polarized 6Li," *Phys. Rev. Lett.* **76** (Jan, 1996) 10–13.

[19] C. Chin, M. Bartenstein, A. Altmeyer, S. Riedl, S. Jochim, J. H. Denschlag, and R. Grimm, "Observation of the Pairing Gap in a Strongly Interacting Fermi Gas," *Science* **305** (2004), no. 5687, 1128–1130.

[20] M. W. Zwierlein, J. R. Abo-Shaeer, A. Schirotzek, C. H. Schunck, and W. Ketterle, "Vortices and superfluidity in a strongly interacting Fermi gas," *Nature* **435** (2005) 1047.

[21] M. Taglieber, A.-C. Voigt, F. Henkel, S. Fray, T. W. Hänsch, and K. Dieckmann, "Simultaneous magneto-optical trapping of three atomic species," *Physical Review A (Atomic, Molecular, and Optical Physics)* **73** (2006), no. 1, 011402.

[22] M. Taglieber, *Quantum Degeneracy in an Atomic Fermi-Fermi-Bose Mixture*. PhD thesis, Ludwig-Maximilians-Universität München, 2008.

[23] A.-C. Voigt, M. Taglieber, L. Costa, T. Aoki, W. Wieser, T. W. Hänsch, and K. Dieckmann, "Ultracold Heteronuclear Fermi-Fermi Molecules," *Physical Review Letters* **102** (2009), no. 2, 020405.

[24] L. Pollet, J. D. Picon, H. Buechler, and M. Troyer, "Supersolid phase with cold polar molecules on a triangular lattice," *preprint arXiv:0906.2126* (2009).

[25] P. Fulde and R. A. Ferrell, "Superconductivity in a Strong Spin-Exchange Field," *Phys. Rev.* **135** (1964), no. 3A, A550–A563.

[26] A. I. Larkin and Y. N. Ovchinnikov, "Superconductivity in a Strong Spin-Exchange Field," *Zh. Eksp. Teor. Fiz.* **47** (1964) 1136; translation: Sov. Phys. –JETP 20 (1965) 762.

[27] M. I. Mizushima, T. and K. Machida, "Fulde-Ferrell-Larkin-Ovchinnikov states in a superfluid Fermi gas," *Journal of Physics and Chemistry of Solids* **66** (2005), no. 8-9, 1359–1361.

[28] T. Fukuhara, Y. Takasu, M. Kumakura, and Y. Takahashi, "Degenerate Fermi Gases of Ytterbium," *Phys. Rev. Lett.* **98** (2007), no. 3, 030401.

[29] R. Chicireanu, A. Pouderous, R. Barbé, B. Laburthe-Tolra, E. Maréchal, L. Vernac, J.-C. Keller, and O. Gorceix, "Simultaneous magneto-optical trapping of bosonic and fermionic chromium atoms," *Physical Review A (Atomic, Molecular, and Optical Physics)* **73** (2006), no. 5, 053406.

[30] A. D. Ludlow, M. M. Boyd, T. Zelevinsky, S. M. Foreman, S. Blatt, M. Notcutt, T. Ido, and J. Ye, "Systematic Study of the [sup 87]Sr Clock Transition in an Optical Lattice," *Physical Review Letters* **96** (2006), no. 3, 033003.

[31] S. Blatt, A. D. Ludlow, G. K. Campbell, J. W. Thomsen, T. Zelevinsky, M. M. Boyd, J. Ye, X. Baillard, M. Fouché, R. L. Targat, A. Brusch, P. Lemonde, M. Takamoto, F.-L. Hong, H. Katori, and V. V. Flambaum, "New Limits on Coupling of Fundamental Constants to Gravity Using [sup 87]Sr Optical Lattice Clocks," *Physical Review Letters* **100** (2008), no. 14, 140801.

[32] T. Loftus, J. R. Bochinski, and T. W. Mossberg, "Simultaneous multi-isotope trapping of ytterbium," *Phys. Rev. A* **63** (2001), no. 5, 053401.

[33] T. Fukuhara, Y. Takasu, M. Kumakura, and Y. Takahashi, "Degenerate Fermi Gases of Ytterbium," *Physical Review Letters* **98** (2007), no. 3, 030401.

[34] M. Petersen, R. Chicireanu, S. T. Dawkins, D. V. Magalhaes, C. Mandache, Y. L. Coq, A. Clairon, and S. Bize, "Doppler-Free Spectroscopy of the [sup 1]S[sub 0]-[sup 3]P[sub 0] Optical Clock Transition in Laser-Cooled Fermionic Isotopes of Neutral Mercury," *Physical Review Letters* **101** (2008), no. 18, 183004.

[35] K.-A. Brickman, M.-S. Chang, M. Acton, A. Chew, D. Matsukevich, P. C. Haljan, V. S. Bagnato, and C. Monroe, "Magneto-optical trapping of cadmium," *Physical Review A (Atomic, Molecular, and Optical Physics)* **76** (2007), no. 4, 043411.

[36] E. Wille, F. M. Spiegelhalder, G. Kerner, D. Naik, A. Trenkwalder, G. Hendl, F. Schreck, R. Grimm, T. G. Tiecke, J. T. M. Walraven, S. J. J. M. F. Kokkelmans,

E. Tiesinga, and P. S. Julienne, "Exploring an Ultracold Fermi-Fermi Mixture: Interspecies Feshbach Resonances and Scattering Properties of ^{6}Li and ^{40}K," *Physical Review Letters* **100** (2008), no. 5, 053201.

[37] E. Tiesinga, A. J. Moerdijk, B. J. Verhaar, and H. T. C. Stoof, "Conditions for Bose-Einstein condensation in magnetically trapped atomic cesium," *Phys. Rev. A* **46** (1992), no. 3, R1167–R1170.

[38] C. R. Monroe, E. A. Cornell, C. A. Sackett, C. J. Myatt, and C. E. Wieman, "Measurement of Cs-Cs elastic scattering at T=30 μK," *Phys. Rev. Lett.* **70** (1993), no. 4, 414–417.

[39] J. L. Roberts, *Bose-Einstein Condensates with Tunable Atom-atom Interactions: The First Experiments with ^{85}Rb BECs*. PhD thesis, University of Colorado, 2001.

[40] H. Wu and C. Foot, "Direct simulation of evaporative cooling," *J. Phys. B* **29** (1996) L321.

[41] G. M. Kavoulakis, C. J. Pethick, and H. Smith, "Relaxation Processes in Clouds of Trapped Bosons above the Bose-Einstein Condensation Temperature," *Phys. Rev. Lett.* **81** (1998), no. 19, 4036–4039.

[42] G. M. Kavoulakis, C. J. Pethick, and H. Smith, "Collisional relaxation in diffuse clouds of trapped bosons," *Phys. Rev. A* **61** (2000), no. 5, 053603.

[43] B. DeMarco, J. L. Bohn, J. P. Burke, M. Holland, and D. S. Jin, "Measurement of p-Wave Threshold Law Using Evaporatively Cooled Fermionic Atoms," *Phys. Rev. Lett.* **82** (1999), no. 21, 4208–4211.

[44] J. Goldwin, S. Inouye, M. L. Olsen, B. Newman, B. D. DePaola, and D. S. Jin, "Measurement of the interaction strength in a Bose-Fermi mixture with $Rb87$ and $K40$," *Phys. Rev. A* **70** (2004), no. 2, 021601.

[45] J. Goldwin, *Quantum Degeneracy and Interactions in the ^{87}Rb-^{40}K Bose-Fermi-Mixture*. PhD thesis, University of Colorado, 2005.

[46] J. J. Sakurai, *Modern Quantum Mechanics*. Addison-Wesley, New York, 1994.

[47] C. Cohen-Tannoudji, B. Diu, and F. Laloe, *Quantum Mechanics (Two Volumes)*. Wiley-Interscience, New York, NY, 1977.

[48] F. Reif, *Fundamentals of Statistical and Thermal Physics*. McGraw Hill International Editions, 1965.

[49] F. Schwabl, *Quantenmechanik, 7. Auflage*. Springer, Berlin, 2007.

[50] W. Ketterle and M. W. Zwierlein, "Making, probing and understanding ultracold Fermi gases," 2008.

[51] S. Giorgini, L. P. Pitaevskii, and S. Stringari, "Theory of ultracold atomic Fermi gases," *Reviews of Modern Physics* **80** (2008), no. 4, 1215.

[52] D. A. Butts and D. S. Rokhsar, "Trapped Fermi gases," *Phys. Rev. A* **55** (1997), no. 6, 4346–4350.

[53] W. Pauli, "The Connection Between Spin and Statistics," *Phys. Rev.* **58** (1940), no. 8, 716–722.

[54] C. J. Pethick and H. Smith, *Bose-Einstein Condensation in Dilute Gases, 2nd Ed.* Cambridge University Press, Cambridge, UK, 2008.

[55] L. H. Thomas, "The calculation of atomic fields," *Proc. Camb. Philos. Soc.* **23** (1928) 542.

[56] E. Fermi, "Eine statistische Methode zur Bestimmung einiger Eigenschaften des Atoms und ihre Anwendung auf die Theorie des periodischen Systems der Elemente," *Zeitschrift für Physik* **48** (1928) 73.

[57] F. Schwabl, *Statistische Mechanik*. Springer, Berlin, 2006.

[58] D. Lüst, *Quantenmechanik (Vorlesungsskript)*. LMU München.

[59] E. P. Wigner, "On the Behavior of Cross Sections Near Thresholds," *Phys. Rev.* **73** (1948), no. 9, 1002–1009.

[60] A. Derevianko, J. F. Babb, and A. Dalgarno, "High-precision calculations of van der Waals coefficients for heteronuclear alkali-metal dimers," *Phys. Rev. A* **63** (Apr, 2001) 052704.

[61] A. Derevianko, W. R. Johnson, M. S. Safronova, and J. F. Babb, "High-Precision Calculations of Dispersion Coefficients, Static Dipole Polarizabilities, and Atom-Wall Interaction Constants for Alkali-Metal Atoms," *Phys. Rev. Lett.* **82** (1999), no. 18, 3589–3592.

[62] Z.-C. Yan, J. F. Babb, A. Dalgarno, and G. W. F. Drake, "Variational calculations of dispersion coefficients for interactions among H, He, and Li atoms," *Phys. Rev. A* **54** (1996), no. 4, 2824–2833.

[63] A. E. Siegman, *Lasers*. University Science Books, Sausalito, CA, 1986.

[64] E. L. Raab, M. Prentiss, A. Cable, S. Chu, and D. E. Pritchard, "Trapping of Neutral Sodium Atoms with Radiation Pressure," *Phys. Rev. Lett.* **59** (Dec, 1987) 2631–2634.

[65] D. E. Pritchard, E. L. Raab, V. Bagnato, C. E. Wieman, and R. N. Watts, "Light Traps Using Spontaneous Forces," *Phys. Rev. Lett.* **57** (Jul, 1986) 310–313.

[66] A. L. Migdall, J. V. Prodan, W. D. Phillips, T. H. Bergeman, and H. J. Metcalf, "First Observation of Magnetically Trapped Neutral Atoms," *Phys. Rev. Lett.* **54** (Jun, 1985) 2596–2599.

[67] T. Bergeman, G. Erez, and H. J. Metcalf, "Magnetostatic trapping fields for neutral atoms," *Phys. Rev. A* **35** (Feb, 1987) 1535–1546.

[68] R. Grimm, M. Weidemuller, and Y. B. Ovchinnikov, "Optical dipole traps for neutral atoms," *MOLECULAR AND OPTICAL PHYSICS* **42** (2000) 95.

[69] J. D. Jackson, *Classical Electrodynamics, 3rd Ed.* John Wiley & Sons, Inc., Hoboken, NJ, 1998.

[70] W. Wieser, "An optical dipole trap for ultracold bosons and fermions," 2006.

[71] J. Goldwin, S. Inouye, M. L. Olsen, and D. S. Jin, "Cross-dimensional relaxation in Bose-Fermi mixtures," *Phys. Rev. A* **71** (2005), no. 4, 043408.

[72] R. V. Hogg and A. T. Craig, *Introduction to Mathematical Statistics*. Prentice Hall, Englewood Cliffs, NJ, 1995.

[73] D. Guéry-Odelin, F. Zambelli, J. Dalibard, and S. Stringari, "Collective oscillations of a classical gas confined in harmonic traps," *Phys. Rev. A* **60** (1999), no. 6, 4851–4856.

[74] A.-C. Voigt, "Simultanes Fangen von drei Atomsorten in einer magnetooptischen Falle," 2004.

[75] F. Henkel, "Fermionisches Kalium in der dreikomponentigen magnetooptischen Falle," 2005.

[76] M. Greiner, "Magnetischer Transfer von Atomen - Ein Weg zur einfachen Bose-Einstein-Kondensation," 2000.

[77] C. Eigenwillig, "Optimierte Herstellung einer ultrakalten Bose-Fermi-Mischung in der Magnetfalle," 2007.

[78] M. Taglieber, A.-C. Voigt, T. Aoki, T. W. Hänsch, and K. Dieckmann, "Quantum Degenerate Two-Species Fermi-Fermi Mixture Coexisting with a Bose-Einstein Condensate," *Physical Review Letters* **100** (2008), no. 1, 010401.

[79] B. DeMarco, S. B. Papp, and D. S. Jin, "Pauli Blocking of Collisions in a Quantum Degenerate Atomic Fermi Gas," *Phys. Rev. Lett.* **86** (2001), no. 24, 5409–5412.

[80] R. Jáuregui, "Nonperturbative and perturbative treatments of parametric heating in atom traps," *Phys. Rev. A* **64** (2001), no. 5, 053408.

Danksagung

Zum Gelingen dieser Arbeit haben direkt und indirekt eine ganze Reihe von Menschen beigetragen. Bei ihnen möchte ich mich an dieser Stelle sehr herzlich bedanken.

Herrn Prof. Dr. Theodor W. Hänsch danke ich sehr herzlich für seine ansteckende Begeisterung und seine spielerische Freude an der Physik - und für die Chance, in seiner Gruppe mitarbeiten zu dürfen.

Herrn Prof. Dr. Stefan Kehrein danke ich für die freundliche Bereitschaft, diese Arbeit als Zweitgutachter zu betreuen.

Meinem Gruppenleiter Dr. Kai Dieckmann danke ich für die interessante Themenstellung, die es mir ermöglicht hat, Theorie und Experiment zu kombinieren, und für die konstruktive Zusammenarbeit. Ich wünsche Dir alles Gute, ganz egal wohin die Reise am Ende gehen wird!

In den ersten Monaten meiner Arbeit hatte ich das große Glück und Vergnügen mit Matthias Taglieber zusammenzuarbeiten, der von der ersten Stunde an als Doktorand an unserem Experiment beteiligt war und uns vor seinem Wechsel in die freie Wirtschaft noch ein paar Monate als Postdoc und Sonnenschein erhalten geblieben ist. Ich habe in dieser Zeit unglaublich viel von ihm gelernt und stelle mir sogar jetzt noch häufig die Frage "Was würde der Matthias jetzt machen?", wenn ich einem neuen Problem gegenüberstehe. Hab ganz, ganz lieben Dank für die Starthilfe!

Arne-Christian Voigt hat es bis zum Schluss nicht aufgegeben, mich von der Qualität des Mensaessens überzeugen zu wollen. Oft geschafft hat er es nicht, aber dafür war er stets angenehme Gesellschaft beim gemeinsamen Espresso im Kampf gegen das Mittagstief.

Hannes Brachmann danke ich ganz herzlich für die angenehme Zusammenarbeit, für die Betreuung beim Zusammenschreiben, für die verlässliche Versorgung mit Schokolade und Butterbrezn und für meine ersten Surfversuche, die auch auf seinem Anfängerbrett unternehmen durfte. Ich drücke Dir die Daumen und wünsche Dir alles Gute für die Doktorarbeit.

Mein Mitdiplomand Matthias Mang war der beste und drolligste Bürokollege, den ich mir nur wünschen konnte. Ohne ihn hätte ich auf viele heitere Momente in diesem Jahr verzichten müssen. Mach weiter so und bleib so humorvoll und fröhlich wie Du bist!

Den Mitgliedern der Treulein-Gruppe danke ich dafür, dass sie es so wohlwollend geduldet haben, wenn wir mal wieder ihr Equipment geplündert haben... Ich wusste lange Zeit wirklich nicht, dass unser Powermeter eigentlich Euch gehört! Ganz besonders gefreut

habe ich mich über die zeitweilige Aufnahme in die legendäre Kuchenrunde. Ich danke Philipp Treutlein für sein ansteckendes Lachen. Stephan Camerer danke ich für bereichernde Diskussionen über den Sinn und Unsinn des Lebens und für vergnügliche Tandemfahrten vom MPQ zurück in die Innenstadt, Max Riedel für ausgezeichnete Cocktails und viele nette Momente. Ich freu' mich schon auf unsere nächste jam session! Maria Korppi ist in der Endphase meiner Arbeit zu uns gestoßen und ist mir durch ihren Humor und ihre nette Art schnell ans Herz gewachsen. Auch den Mitgliedern der Weinfurter-Gruppe, insbesondere Daniel, Michael, Juliane und Florian möchte ich ganz herzlich danken für gute Nachbarschaft, nette Kaffeepausen und das ein oder andere Kuchenstück. Toni Scheich danke ich herzlich für geduldige Elektronikerklärungen noch zu meinen HiWi-Zeiten und für die vielen Mon Chérie zwischendurch. Gabriele Gschwendtner und Nicole Schmidt haben sie um die ganzen organisatorischen Dinge gekümmert und uns somit die Arbeit erleichtert.

Mit der Garchinger Hänsch-Gruppe war das Gruppenseminar auf Schloss Ringberg ein ein schönes Erlebnis, das mir in guter Erinnerung bleiben wird.

Meinem alten Freund Chandra danke ich für musikalische Leckerbissen und bereichernde Physikdiskussionen, in denen er mir immer wieder gezeigt hat, wie wichtig es ist, simple Fragen zu stellen, und wie weit man mit ein paar einfachen Grundannahmen kommt...

My absolutely amazing friend Simon is the fastest und most talented proofreader I could have wished for. Thank you for your comments from the theorist's point of view and for the many subtleties of the English language you pointed out.

Jon Goldwin very quickly replied to my questions regarding his work and gave me some helpful insight. Thanks a lot!

Nadine, Fridl, Felicia, Lisa, Anni, Jörg, Jens, Ralf, Patrick, Constanze und Sebastian, Euch danke ich einfach dafür, dass es Euch gibt!

Ein allergrößte Dankeschön gilt meiner Familie und ganz besonders meinen Eltern. Ihr habt mich mein Leben lang in all meinen Interessen und Aktivitäten vorbehaltslos gefördert und unterstützt, auch als ich (ausgerechnet!) Physik studieren wollte - dafür kann ich Euch gar nicht genug danken. Ihr seid die besten Eltern, die es gibt! Mein Schatz war, wann immer es ging, für mich da und hat mich sehr unterstützt und aufgemuntert in den letzten Monaten. Ein ganz liebes Dankeschön für alles!

Die Konrad-Adenauer-Stiftung hat mich während meiner gesamten Studienzeit finanziell und vor allem ideell gefördert, wofür ich sehr dankbar bin. Die unzähligen und thematisch so vielfältigen Seminare, an denen ich teilnehmen durfte, waren für mich eine Art Studium Generale, die dort entstandenen Freundschaften eine große Bereicherung. Ich werde immer gern an die Begegnungen an Orten wie Schloss Eichholz, Wendgräben und Cadenabbia zurückdenken.

Erklärung

Hiermit erkläre ich, dass ich diese Arbeit selbständig verfasst und keine anderen als die angegebenen Quellen und Hilfsmittel benutzt habe.

Datum	Unterschrift